Constrained Sintering Of Gold Circuit Films On Rigid Substrates

by

JoonWon Choe

Thesis submitted to the faculty of the

Virginia Polytechnic Institute and State University

in partial fulfillment of the requirements for the degree of
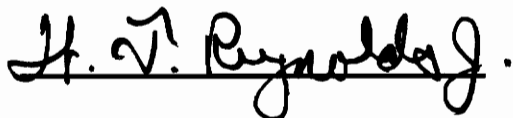
MASTER OF SCIENCE

in

Materials Science & Engineering

APPROVED:

Guo-Quan Lu, Chairman

W.T. Reynolds Jr.   A. Elshabini-Riad

July, 1994

Blacksburg, Virginia

Constrained Sintering Of Gold Circuit Films On Rigid Substrates

by

JoonWon Choe

Committee Chairman: Guo-Quan Lu

Materials Science & Engineering Department

(ABSTRACT)

The densification behavior of porous gold films made from commercial circuit paste used in microelectronic packaging applications was studied. Constrained gold circuit films of 60-65μm thick were formed by multiple screen printing of the gold paste on rigid alumina substrates, while freestanding films were obtained by carefully peeling off gold films from the substrates after binder burn-out. Optical techniques were developed to determine the densification kinetics of the constrained and freestanding films at temperatures below $1000^{\circ}C$. The densification kinetics of gold films constrained on rigid substrates were observed to be significantly retarded relative to the free films, at all sintering temperatures between $650^{\circ}C$ and $900^{\circ}C$ studied. SEM studies revealed the microstructure of the constrained-films to be much more porous than its freestanding film counterpart. Considerably higher sintering temperatures were required to obtain densities comparable to those of freestanding films. SEM studies also showed no significant difference in grain size between the sintered freestanding and constrained gold films. In-plane tensile stresses generated during constrained-film sintering, was determined to have a maximum value of 460 KPa at the sintering temperature of $750^{\circ}C$. The negligible difference in grain size between the sintered freestanding and constrained gold films, and

the small magnitude of the measured tensile stresses, were both determined to be insufficient to account for the observed retardation in the densification kinetics of the constrained gold films. The activation energies for densification of the porous gold films during isothermal sintering, were found to be 21.54 ± 1.03 Kcal/mole and 45.12 ± 1.6 Kcal/mole for freestanding and constrained gold films respectively. These values corresponded very well with the activation energies for grain-boundary diffusion and lattice diffusion respectively, for gold as found in literature. Hence from our results of the activation energies for densification of the constrained and freestanding gold films, coupled with our studies on grain growth and stress, we suggest that the observed retardation in the densification kinetics of the constrained gold films are due to a change in the dominant diffusion mechanism during sintering of the porous gold films constrained on rigid substrates.

ACKNOWLEDGMENTS

TABLE OF CONTENTS

LIST OF FIGURES

LIST OF TABLES

CHAPTER I

INTRODUCTION

Multilayer ceramic substrates constructed from metal and ceramic layers are commonly used as substrates for advanced electronic packages. Continuous trends towards an ever-increasing performance and circuit/bit densities of today's semiconductor chips, have placed greater demands on the performance of the ceramic packages. The multilayer ceramic chip carrier has become the major technology in fabricating such packages, which not only serves as electrical interconnecting substrates for integrated circuit (IC) chips, but also provides the semiconductor chips with mechanical support as well as the means to dissipate heat away from the chips.

The traditional method of manufacturing multilayer ceramic substrates, involved the sequential sintering of the insulator layer, the dielectric layer, and the metallization layer separately. Due to the growing need for high density, high speed packages, reliability becomes the only limitation in the number of layers in a single multilayer substrate. It is also considered to be not economical from the processing point of view, to sinter more than 10 layers of different materials separately. Hence in order to reduce both the cost as well as the time in the manufacture of multilayer ceramic substrates, multilayer co-sintering technology has been developed. Although the co-sintering process has many obvious advantages over the conventional sequential sintering process, it has also been known to be a more complicated process requiring more careful control of the processing conditions.

The manufacturing process of the multilayer cofired ceramic packages involves laminating multiple ceramic green sheets, each having an unique metal ink circuit pattern, and then cosintering at high temperatures [1]. The two types of porous materials in

1

general have significantly mismatched densification kinetics during the cosintering process [2], whereby one material undergoes rapid densification while the densification in the other has not begun. Hence the porous materials are to a large extent constrained from sintering by one another in the plane of the multilayer structure. In the fabrication of hybrid electronic packages, porous metal ink films and inorganic dielectric green layers are constructed on rigid substrates and then sintered together at high temperatures [3]. During the sintering process, the porous materials are constrained from shrinking in the substrate plane and densifies mainly by shrinking normal to the substrate.

Constrained-film sintering is considered to be the most critical issue in both technologies due to the formation of defects during processing. Common defects in hybrid packages are [3] high porosity in the sintered films, and delamination or cracking at the film/substrate interface. While in the multilayer cofired ceramic packages, part distortion or camber and via defects [4] are some major concerns to the manufacturers. These defects have been known to significantly reduce both the performance, as well as production yields.

There are however few published studies on constrained-film sintering [50-53], of which only the work of Garino and Bowen [51] includes experimental data. They measured the densification kinetics of freestanding and constrained glass and ceramic films. Due to the lack of a suitable equipment in their measurements, they had to weigh micrographs taken during the sintering of a free film on a hot stage inside a SEM in order to determine its densification kinetics. To measure the constrained-film kinetics, they determined the film thickness shrinkage profile by an elegant laser reflection technique and an optical microscope. The constrained-films were sintered inside a resistance-heated furnace different from the SEM hot stage in which the free films were sintered. This makes the temperature calibration between the two furnaces, which may not be easy, a critical concern when comparing the two densification kinetics. Also, their way of

determining the densification kinetics of free films by weighing micrograph papers does not appear to be very practical and accurate method. We think that it has been this lack of suitable techniques that has hindered the accurate measurements of densification kinetics of porous films. Recently, we developed an optical technique capable of measuring accurate linear shrinkage profiles of freestanding ceramic green tapes and metal ink films. We also constructed another optical system based on the technique similar to but less cumbersome than that used by Garino and Bowen to determine the densification kinetics of constrained-films. An entirely different optical system was also constructed to measure the magnitude of in-plane tensile stresses developed during sintering of constrained porous gold films. To our knowledge, there has not been any experimental work done to measure the magnitude of the internal stresses generated during constrained sintering of a porous body.

Hence the first goal of the present research, was to use the new experimental techniques developed to measure the densification kinetics of constrained porous gold circuit films, and to compare the results with the measured densification kinetics of the freestanding films. A technological significance of this research effort, would be to use this basic knowledge so as to guide packaging engineers in their materials selection process and processing optimization, hence improving production yield. The second goal of the present research, was to successfully measure the in-plane tensile stresses developed during constrained sintering of porous gold films. This result is considered to be very important in understanding the formation of camber, due to the generation of in-plane tensile stresses during the co-sintering of the multilayer structures.

In the following chapter, a literature review of the processing of multilayer ceramic packages will be presented. An important aspect of the processing step, the co-sintering stage, will be examined in greater detail by reviewing the current understanding of the

sintering behavior, as well as by reviewing the differential sintering behavior of porous materials.

New experimental techniques developed to measure the densification kinetics of freestanding porous gold films, and porous gold films constrained on rigid substrates through the use of different laser-optical setups, will be presented in Chapter 3. This Chapter will also present a description of the sample preparation techniques, as well as the experimental technique used to measure the in-plane tensile stresses developed during constrained sintering of porous gold films.

The results on the measurements of the densification kinetics of the freestanding and the constrained porous gold films will be presented in Chapter 4. The results of this work is of great interest, since a basic understanding on the kinetics of constrained-film sintering and how it differs from the densification kinetics of freestanding films, would better explain the mechanisms responsible for the formation of defects. Chapter 4 will also present the results on the measurement of the in-plane tensile stresses developed during constrained-film sintering.

In Chapter 5, a discussion of the results will be presented. In this Chapter, the experimental measurement on the in-plane tensile stresses developed during constrained-film sintering, will be compared with the internal hydrostatic stress values predicted by various authors using different models. The experimental results on the in-plane tensile stresses coupled with SEM studies on the grain growth kinetics during sintering of freestanding and constrained gold films, would then be used to explain the measured difference in the densification kinetics of the freestanding and the constrained porous gold films.

A summary and a conclusion of this thesis work, as well as some of the future works that could be done, will be presented in Chapter 6.

CHAPTER II

LITERATURE REVIEW

2.1   Review of the Multilayer Ceramic Processing

The increasing demand on ceramic chip packages to be able to deliver both an increased amount of power, and an increased number of interconnections to chips in a manner which allows removal of the increased heat dissipated, has put forth a stage that has embraced the development of the multilayer ceramic technology. The monolithic construction was only limited to multilayer capacitors amongst the electronic products in the 1960's, but the potential for high volume efficiencies as well as improvements in strength and thermal conductivity has led to extensive development of the multilayer technology to most electronic products. The earlier processing techniques used in manufacturing ceramic-metal laminates, involved : (a) bonding of sintered and metallized ceramic plates, (b) sequential layering of ceramic and metal powders followed by sintering and (c) gas phase formation on a sintered substrate. This processing technique was however deemed to be highly inefficient in terms of quality, production yield and cost, especially for applications requiring many insulating layers with separate thicknesses ranging from 25 to 500 microns. Studies conducted by Schwartz and Wilcox [5] during the sixties on the specific features of a desired ceramic manufacturing process included, (a) separate formation of individual layer, (b) lamination of layers in the green state, (c) elimination of differential shrinkage, and (d) a single heating cycle. The "Multilayer-Ceramic" technology has not only met the objectives as stated above, but improvements of every phase of the multilayer-ceramic technology as been made in recent years. The improvements in the multilayer-ceramic technology has led to the development of very complicated high performance multilayer structures, such as the "State-of-the-Art" thermal

conduction module which is capable of interconnecting in excess of 30 ceramic layers, with 30 layers of metal to support devices in excess of 100 chips on a single substrate [1].

A schematic of a typical multilayer ceramic fabrication process is shown in Figure 2.1. First, thin and flat ceramic sheets are made by tape casting using doctor-blades, then holes are punched in the individual ceramic sheets to obtain the desired forms. Metallization of desired conduction circuitry patterns are then screen printed onto the ceramic sheets, followed by laminating many of the metallized ceramic sheets together. The final shapes required are then punched out from the laminated ceramic sheets, which are then sintered to obtain the final monolithic part with both internal and surface conductors. Since defects introduced in any one stage of the fabrication process are retained in the final multilayer structure, careful control of the parameters are required in each processing step. In the following sections, each of the individual processing steps for the fabrication of the multilayer ceramic structure will be reviewed.

2.1.1 Green Sheet Preparation - Tape Casting

The basic building block used in the multilayer ceramic process is the "ceramic green-sheet", nominally with a thickness in the range of 25 to 1250 microns, which is a mixture of ceramic and glass powder suspended in an organic binder. The most common method of forming a green sheet, is through the tape casting process (or doctor-blading). The tape casting process consists basically of suspending finely divided inorganic powders in aqueous or non aqueous liquid systems comprised of solvents, plasticizers, deflocculents and binders to form a slurry that is cast onto a moving carrier surface. The slurry passes beneath the knife edge of a blade that levels the slurry into a layer of controlled thickness and width as the carrier surface advances along a supporting table. When the solvents evaporate, the fine solid particles coalesce into a relatively dense flexible sheet [6]. A key factor in achieving acceptable yields, is the formulation of a

Cast	Form	Print

Ceramic Slurry

Punch   Laminate

Co-Sinter
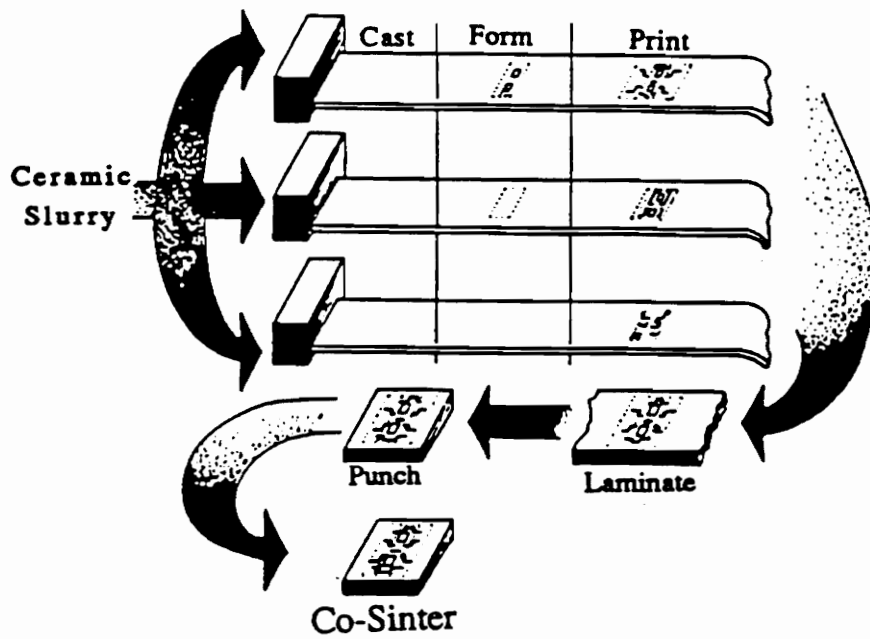
Fig.2.1   Schematic of a typical multilayer fabrication process.

(After Gardner and Nufer [26])

green-sheet that exhibits the necessary strength for handling and processing. In addition, the green-sheet must be dimensionally stable to ensure accurate plane-to-plane registration when the layers are stacked and laminated. Strength and stability have been achieved by the proper selection of binder constituents, a controlled casting process, and the use of a molybdenum paste vehicle that does not interact with green-sheet binder.

2.1.2 Punching

The as-cast sheets of ceramic are cut to the desired sizes and shapes with a simple punch and die set actuated by a rotary punch press. This operation is called ' blanking '. The pieces are usually punched oversize to allow for sintering shrinkage. Higher precision can be achieved by using computer-controlled step and repeat equipment to punch via holes in each green-sheet layer. A pallet, used for mounting the green-sheets, is an integral part of a precision x-y table that moves the green-sheet relative to a stationary die set containing 100 punches at a rate of approximately ten steps per second. A location hole in each corner of the green-sheet is used to position the green-sheet on the punch pallet. Up to 36,000 via holes are punched in a single green-sheet layer. The punch tool also includes an inspection station that contains a light source and an array of photo-diodes to determine the exact location of the hole patterns. If any holes are clogged, the sheet is either repaired or discarded.

Different size and shape holes can also be used for making subsequent electrical connections through the layers, or for leaving cavities in the monolithic structure. Cleanliness of the punch and die are important to prevent introduction of defects onto the substrate surface.

2.1.3 Metallization

The principle method of metallization of the green ceramic sheets is through the process of screen printing as shown in Figure 2.2. Special plate chucks or vacuum chucks are used to hold the green sheets in place. The registration holes position them in regard to the screening masks. When the vacuum chuck is used to hold the green sheets, the suction of the vacuum chuck can also help the screened metal paste fill the via holes to make the electrical connection through layers.

The various steps involved in the screen printing operation is shown in Figure 2.3. The screen printing process is essentially a stencil process in which the printing medium (ink or paste) is forced through the open areas of a mesh-reinforced stencil onto the surface of the green sheets, by passing a rubber blade, called the "squeegee", across the screen. The mesh fabric of the screen performs the dual function of holding together the various parts of the screen and also, by virtue of its thickness, metering the thickness of the ink deposit. During the screen printing process, the screen is held parallel to and slightly above the surface of the green sheet. The separation between the screen and the green sheet, called the "snap-off" distance, varies according to the size and type of the screen, the ink rheology, and the printing conditions being used.

The paste or ink, is applied to the upper surface of the screen and a flexible squeegee is traversed across the pattern area. The passage of the squeegee presses the screen into contact with the green sheet, and forces the paste through the open meshes of the screen. Behind the squeegee the screen, by virtue of its tension, peels away from the green sheet leaving a printed pattern of ink on the surface.

The inks or pastes used for thick film circuit printing consist of a suspension in an organic vehicle of finely divided metals, metal oxides, or a mixtures of these with a glass frit or binder. The paste are deposited on the green sheets so as to perform the functions of conductors, resistors, or dielectrics. Reproducible results with screen printing, requires

Initial Position Of Screen Fabric

Rubber Squeegee

Direction Of Squeegee Traverse

Screen Frame

Ink

Screen Fabric

Substrate
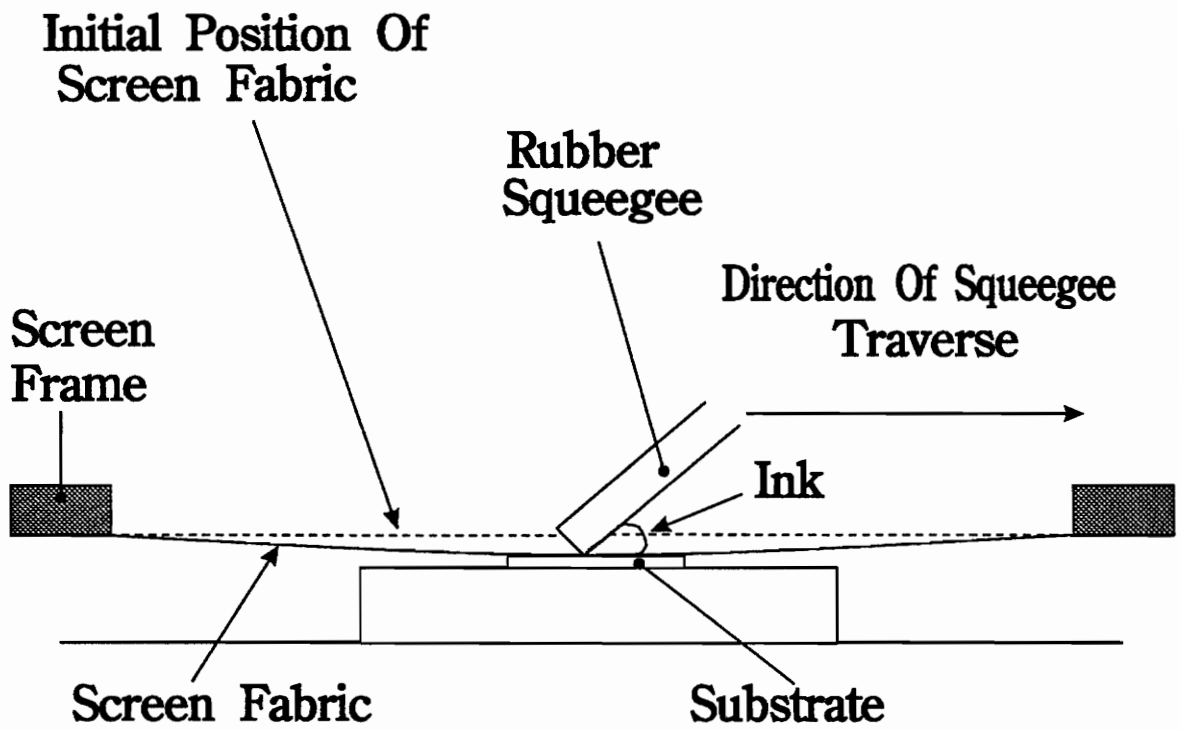
Fig.2.2   Schematic of the basic " off contact " screen process.
(After Holmes and Loasby [3])
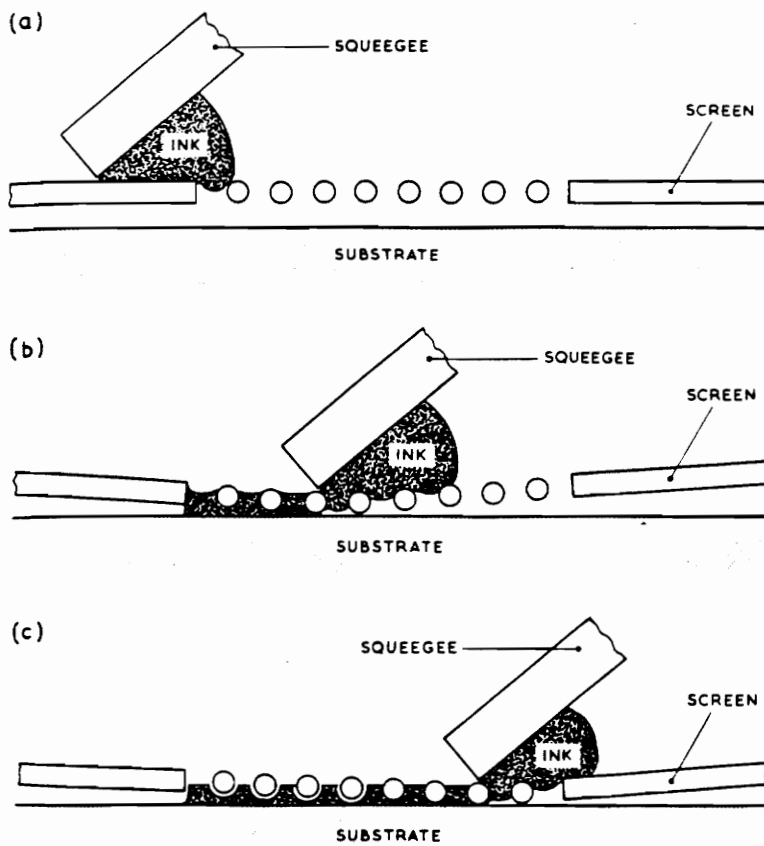
Fig.2.3.   Schematic of a typical screen printing operation.
(After Holmes and Loasby [3])

close control of the paste properties (e.g., viscosity, specific gravity, etc.), screens, and processes.

2.1.4 Lamination

The lamination process is applying pressure to several stacked metallized green sheets at a suitable temperature in order to produce a monolithic structure. The temperature typically ranges from room temperature to several hundred degrees Fahrenheit. Depending on the temperature and the amount of binder in the green sheets, the pressure required during the laminating process varies in the range of 200 to 20000 psi.

Complete lamination is only ensured if the entire surface of the multilayer receives equal pressure. Hence it is important to ensure that the heating plates are highly polished and perfectly parallel during the lamination process, especially when the multilayers have large areas. It is important that sufficient time is given for the entire multilayer structure to reach thermal equilibrium.

Studies have shown that some densification occurs in the multilayer structures during the lamination process. The amount of densification would depend on temperature, pressure, and the duration of the lamination process. Since the density of the green sheets would change after the lamination process, the amount of shrinkage during the sintering stage will also be altered. Hence it is important that the lamination process is carefully controlled, so as to ensure precision dimensional control of the multilayer during sintering.

2.1.5 Final Shaping

This is the final step before the sintering process, where individual parts are removed from the large single laminated green sheets through stamping. To this point, the

individual parts had been processed in a batch, usually on a continuous roll. The previous operations of punching, metallization, and lamination may be repeated on the same material several times in order to obtain unique designs. This repeated processes would allow the fabrication of intricate shapes within the individual parts, before the sintering process.

2.1.6 Sintering

The sintering process is the most complex of all the processes used in the fabrication of the multilayer ceramic substrates. It involves subjecting the green multilayer to a specific temperature-time-atmosphere cycle in order to remove the binders, complete any desirable reactions, densify the structure, complete the bonds between different phases, and control the grain and pore sizes. In this process, the materials shrink uniformly , as part of the densification, which is controlled in a manner similar to any other ceramic or powder metallurgical processing.

The complexity of the sintering process arises from the formation of defects during the densifying process. Although during sintering the multilayers densify as a whole, stresses are generated when shrinkage differs for different components in the multilayers. It is the development of these stresses that causes defects such as bowing, blistering, cracking, and delamination. Pepin et. al. [7] have identified delamination as the more serious of the four defects, and have attributed four causes of delamination in multilayer ceramic capacitors due to the electrode. Firstly, delamination occurs due to the high organic resin contents in the electrode vehicle. Secondly, the green state delamination occurs as a result of the lack of adhesion between the dried electrode print to the dielectric tapes. Thirdly, the catalytic reactions of the electrode precious metals with the organics during binder burnout and sintering have been known to cause delamination. Lastly, the mismatch in the densification kinetics between the electrode and the dielectric have also

been known to cause delamination. Solutions to eliminate the problem due to the first three causes have been suggested, by modifying the electrode paste. Modifying the electrode by reducing the resins in the electrode vehicle, using adhesion promoter to increase the lamination bonding strength, and reducing the electrode powder surface area to avoid catalytic reactions, have been reported to eliminate the problem. Although the solutions to the first three causes were addressed, nothing was mentioned on how to accomplish reduction in differential shrinkage.

Currently, packaging engineers often resort to trial and error solutions to minimize the defect formation by varying the sintering temperature-time profiles, and by varying the particle size distribution of the metallization layer, to obtain close matching of the shrinkages between the metal layer and the ceramic substrate. Since warping of the sintered part and the adhesion of the metallization are greatly dependent on the well matching of the shrinkage between the metal and ceramic layers, an understanding of the different sintering paths taken by the two materials are essential to reduce the defect formation. The different sintering mechanism for glass (viscous flow) and metals (solid state sintering) must be taken into account when attempting to match the shrinking rates. Other important factors such as the amount of binder, powder characterization, purity of materials, accuracy of controls, and the techniques of handling the parts, all contribute to the success of the multilayers.

2.2   Review of Sintering Phenomenology

" Sintering is thermally activated, spontaneous and initiated by outer action of a transfer system of solid bodies in contact or a porous medium into thermodynamic more equilibrium state by area reduction of a free surface. "

(V.V. Skorohod, S.M. Solonin, 1984)

Although mankind has been sintering ceramics and metals for thousands of years, it has only been studied in closer detail since the 1920's. It was not until the middle of this century that extensive publications were made on investigations of the sintering process on simple ceramic oxide systems. The breakthrough in sintering theory achieved by Kuczynski [8] has stood as a benchmark with only relatively minor refinements since. On the other hand, the technology of sintering has made great strides over the same four decades, seemingly without much need for theories. Several ceramic materials have been cold-pressed and sintered to essentially theoretical density while maintaining reasonable grain sizes, while the powder metallurgy industry has produced parts with superior properties compared with wrought products. However, the advances have been more the result of empiricism and trial and error, then through an understanding of the basic science of sintering.

In the sections to follow, some of the important aspects of the sintering theory and practice will be reviewed. A more detailed study of the sintering process can be found in literature [9-11].

2.2.1 Driving Force for Sintering

Everyone agrees that the driving force for the sintering is the excess surface energy of a compact of powder particles, and all sintering phenomena bring about the reduction in the total interfacial energy. The powder particles change their shape by rounding off sharp corners or developing facets at low energy orientations consistent with the constraints placed by contacts with adjacent particles. Necks forming between particles substitute grain-boundary area for surface area, always with a net reduction in total interfacial energy. The resulting network of porosity often is reduced in volume, it often coarsens and eventually loses connectivity as the branches pinch off, giving first blind pores and

finally isolated pores. The isolated pores may continue to shrink slowly or they may grow as grain growth continues.

The final goal of sintering is usually to produce a pore-free body, by being able to transport material to or around the pores during the sintering process. There are two important driving forces which lead to material transport. The first one is the chemical potential gradient. The difference between the chemical potential of an atom under a curved surface of principle radii of curvature r_1 and $r_2(\mu)$ and a flat surface (μ_o) is given by

$$\Delta\mu = \mu - \mu_o = \gamma\Omega\{(1/r_1) + (1/r_2)\} \tag{2.1}$$

where Ω is the atomic volume and γ is the surface energy per unit area. r_1 and r_2 are positive if the surface is convex, and negative if it is concave. This chemical potential gradient also gives rise to a gradient in the vapor pressure above these two surfaces such that

$$\Delta\mu = kT\ln(P/P_o) \tag{2.2}$$

where P is the partial vapor pressure over a curved surface, P_o is the partial vapor surface over a flat surface, k is the Boltzman's constant and T is the absolute temperature.

Thus, the atoms move from the convex to the concave regions to decrease the potential gradient. The vacancies counter-current the diffusion of the atoms and therefore, diffuse away from the contact area between the solid particles and sink at the dislocations or grain boundaries.

The second driving force for material transport is due to the stress generation at the contacts between particles. Considering the geometry of the contacts shown in Figure 2.4, it can be shown that the outer edge of the contact is subjected to a tensile stress, σ, given by [12]

$$\sigma = \gamma\{(1/\rho)-(1/x)\} \tag{2.3}$$
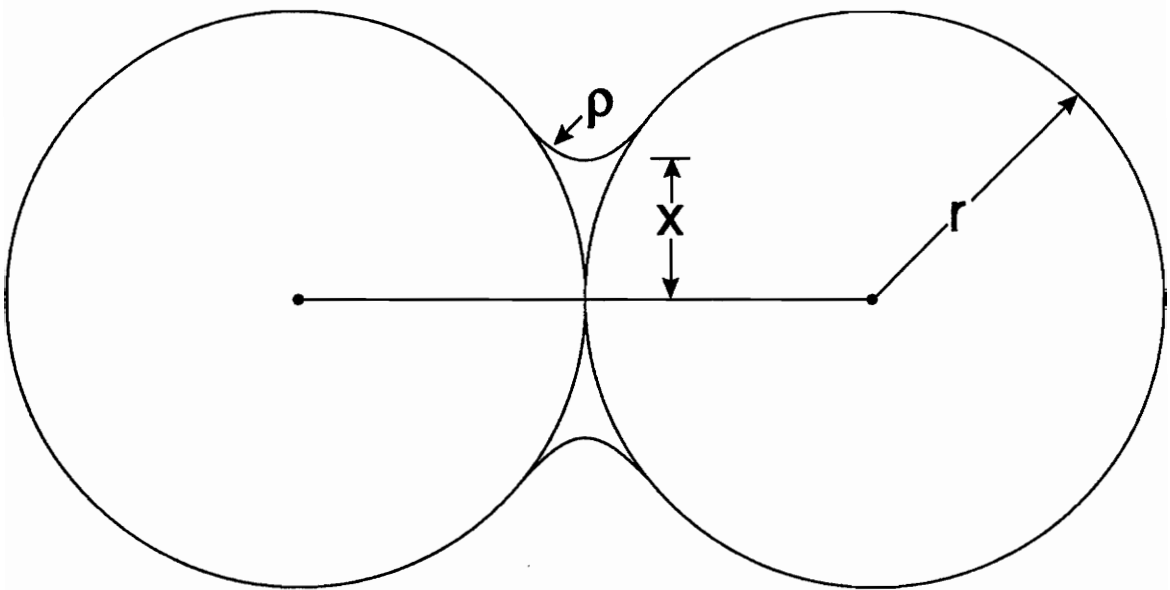
Fig.2.4   Geometry for the initial stages of sintering of two spheres.

where γ is the surface tension. If this stress is greater than the yield stress of the material, material will transport through microscopic viscous or plastic flow.

Although these microscopic material transport mechanisms can be well modeled, in the real sintering of a powder compact, only one physical change can be observed, i.e., the shrinkage of the whole powder compact. Thus, from a macroscopic point of view, the driving force for sintering can be regarded as a " sintering pressure ", which combines the effects of chemical potential gradient, stress, etc. and represents the overall driving force.

Recently, several researchers have performed sinter-forming experiments on powder compacts to determine the sintering pressure [35,36]. Rahman and DeJonghe [35] found that the sintering pressure of CdO powder compacts decreases with increasing density; they attributed the reason to an increase in grain size as density increases. Venkatachari and Raj [36] also found that the sintering pressure of Al_2O_3 powder compacts decreases with increasing density. It decreases from 0.8 MPa at 0.70 relative density to 0.4 MPa at 0.95 relative density.

The sintering pressure was analyzed from a purely thermodynamic point of view by Raj [37]. He derived a simple expression for the sintering pressure as

$$p_o = (2\gamma_b / \Delta) + (2\gamma / r) \tag{2.4}$$

where γ_b is the grain boundary free energy, γ is the surface free energy, Δ is the grain size and r is the radius of curvature of the pore surface. The difference between the sintering of glass material and the sintering of polycrystalline material can be highlighted using equation (2.4). In the sintering of glass, the first term in equation (2.4) will be absent, and the sintering pressure of glass will increase with increasing density, since r will decrease as the porosity is eliminated by sintering. In the sintering of polycrystalline materials, an increase in density is usually accompanied by an increase of grain size,

implying that the sintering pressure may become smaller at higher densities depending upon which term in equation (2.4) dominates.

2.2.2 Stages of Sintering

Three stages sequentially describes the course of sintering. In general, these three stages are not discrete, but overlaps considerably. The most common way to define these stages is in terms of pore and grain morphology. A "stage" is, then the time period during which well-defined changes in pore shape takes place.

The initial stage of sintering corresponds to the state in which the interparticle contact area increased from zero to ≈ 0.2 of the cross-sectional area of the particle. Neck growth takes place between the particles, but the particles remain individual, as shown in Figures 2.5(a) and 2.5(b). The neck growth will be accompanied by interparticle shrinkage of a few percent, whereby densification would increase the relative density from 0.5 to 0.6. A marked decrease in the specific surface area of the compact occurs due to surface smoothing. The point at which grain growth first occurs is considered to terminate the initial stage of sintering.

The intermediate stage of sintering begins after grain growth and is characterized by a more or less continuous network of pore channels along the grain edges as shown in Figure 2.5(c). During this stage, the pore channels shrink while the grain grows. Most of the densification occurs during this stage.

The final stage of sintering begins when the pore channels are eventually pinched off and form isolated spheroidized pores, Figure 2.5(d). The energetically favored structure is that in which the closed (nearly spherical) pores occupy four-grain corners. Each individual pore will continue to shrink at a slower rate until it is completely eliminated.
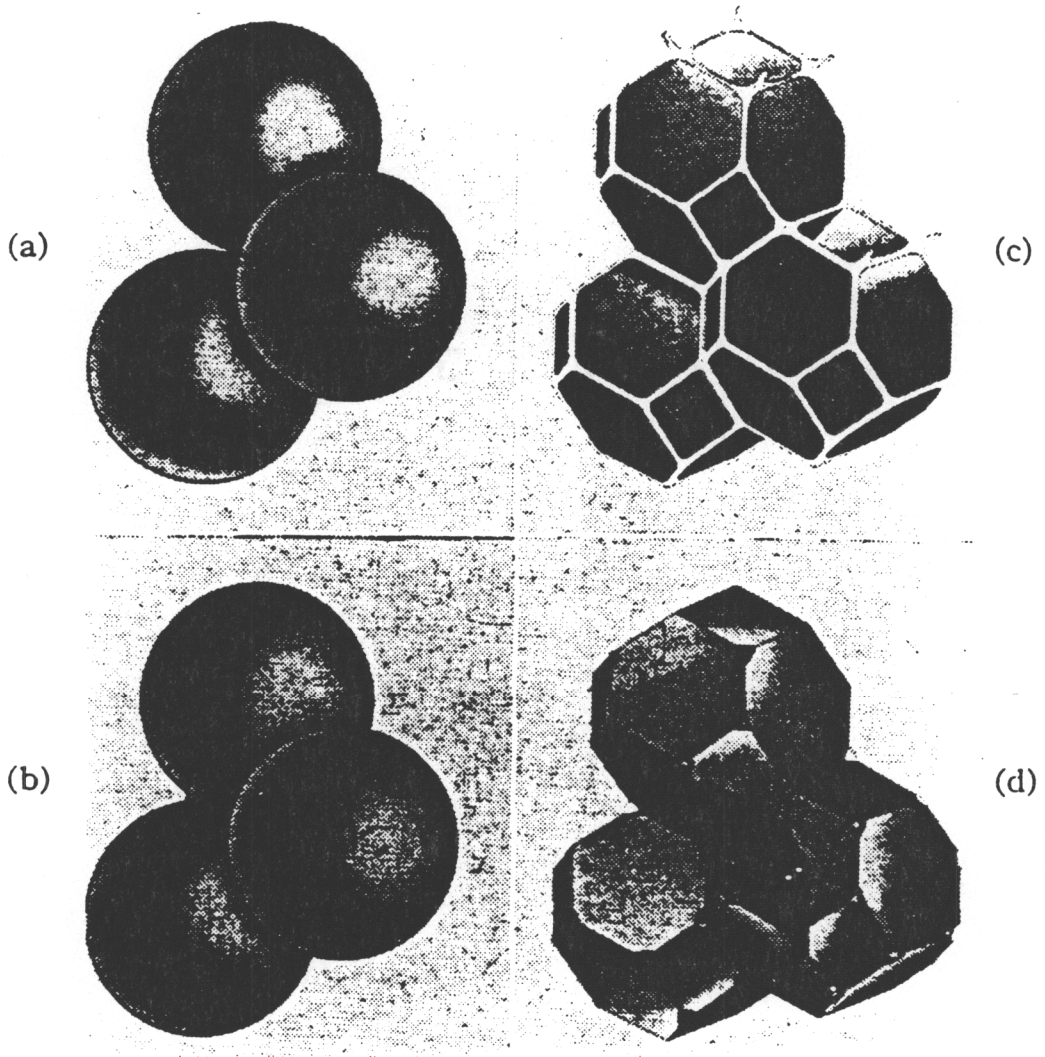
Fig.2.5 Three dimensional illustration of stages of sintering: (a) Initial stage-spheres in tangential contact, (b) Near end of initial stage, necking between particles, (c) Intermediate stage with continuous pore channels at grain edges, (d) Final stage, tetrahedral pores at four grain intersections. (After Coble [14])

2.2.3   Sintering Mechanisms and Models

When a powder aggregate is sintered, necks form between the powder particles, and the aggregate may increase in density. Even in a our, one-component system, at least six distinguishable mechanisms contribute to neck growth and to densification. Most of these involve the diffusive transport of matter to the growing neck; Figure 2.6 shows some of the possible diffusion paths. Table 2.1 shows the sources and sinks of matter for each of these six mechanisms [13].

Numerous models for initial stage solid state sintering have been presented. The various models predict rate equations for neck growth and densification for simple geometries, like a pair of wires or spheres. Ashby [13] have compiled and used these rate equations developed for a single transport mechanism, to construct "sintering maps".

Although there a large number of models for initial stage sintering, the number of models available for the intermediate stage is limited. The models that are available, are normally based on some model of interconnected porosity, and hence give very similar parametric dependence for densification, although the actual numerical values of coefficients differ.

The first notion of modeling intermediate stage microstructure, with porosity modeled as cylinders around the edge of tetrakaidecahedron shaped grains, was introduced by Coble [14]. He calculated the densification rates for volume and grain boundary diffusions separately. Johnson [15] used similar geometry in his model, but also allowed for non-densifying mechanisms such as surface and vapor transport. Johnson [15] also developed the shrinkage rate for combined volume and grain boundary diffusion in terms of surface parameters. Beere [16] made a significant contribution by assuming the pore to have a complex shape and to have met the grain boundary at the correct dihedral angle. He calculated the pore shape by minimizing the surface area for a fixed volume, whereby the calculated densification then depended on the dihedral angle.
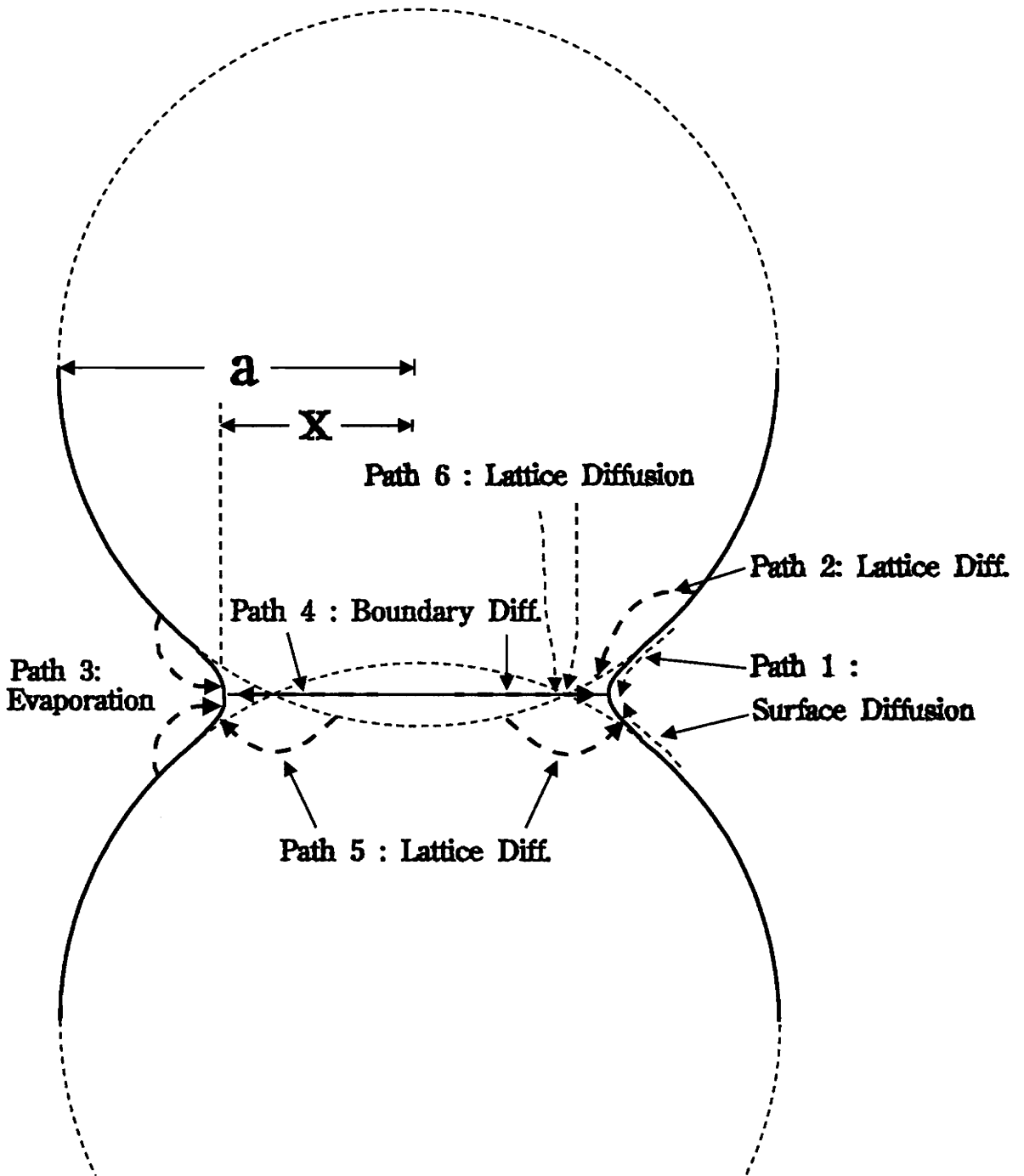
Fig.2.6   Six paths for matter transport. All lead to neck growth. Only
paths 4,5 and 6 cause densification.   (After Ashby [13])

Mechanism No.	Transport path	Source of Atoms	Sink of Atoms	Densification ?
1	Surface Diffusion	Surface	Neck	No
2	Lattice Diffusion	Surface	Neck	No
3	Vapor Transport	Surface	Neck	No
4	Boundary Diffusion	Grain Boundary	Neck	Yes
5	Lattice Diffusion	Grain Boundary	Neck	Yes
6	Lattice Diffusion	Dislocations	Neck	Yes

Table 2.1   The transport paths, sources and sinks of matter and whether densification occurs or not for various initial stage sintering mechanisms. For mechanism numbers, refer to Fig.2.6. (After Ashby [13])

The main weaknesses of these models has been the fact that none of them addressed the issue of grain growth from a fundamental standpoint. Even the geometrical assumption of uniform pores and grain size throughout the sintering body is incorrect. On the grain growth aspect, Coble [14] has introduced an empirical grain growth equation. The equation assumes the volume of the individual grains to be proportional to the sintering time. The well known semi-logarithmic sintering law equation is given by

$$P - P_0 = K \ln(t / t_o) \qquad (2.5)$$

where K contains all physical constants of diffusion sintering and grain growth. P_o and t_o are the porosity and the time at the onset of intermediate stage sintering.

The final stage of sintering is geometrically the simplest. The pores are isolated and assumed to be located at four grain junctions. Again, Coble [14] has calculated the rate of densification for this geometry. The porosity is modeled as equilibrium shaped cavities on the grain boundaries and the densification rate is calculated by deriving the rate of shrinkage of these cavities under the compressive surface tension force.

Other models that have been used for the sintering process, includes the topological model, the rheological model, the empirical and the phenomenological models.

2.3   Review of Differential Sintering

Differential sintering simply means a body containing two or more different regimes that sinter at different rates. Therefore, differential sintering exist not only in the processing multilayer ceramic packages and the processing of composite materials, where two or more different materials sinter at different rates, but also in monoliths where differential sintering could arise due to the presence of aggregates or agglomerates in the powder compacts. In the sections to follow, available analysis to model the differential

sintering phenomenon, as well as experimental results regarding the subject of differential sintering will be given.

2.3.1   Inhomogeneties - Particulate Composites

The effect of inhomogeneties on sintering has been well documented experimentally. The two most important effects are : (a) the generation of defects in the sintered microstructure, and (b) the retardation of the densification kinetics.

The effect of rigid inclusions on the sintering of glass powder compacts were studied by Rahaman and DeJonghe [38]. They reported the sintering of glass-SiC composite as a function of inclusion volume fractions. They found that the densification rates of the composite are in good agreement with the rule of mixture for the inclusion volume fractions of ≤0.1. They calculated the transient stresses caused by the inclusions based on Scherer's theory for viscous sintering with rigid inclusions [39]. The results are in agreement with Scherer's theory for inclusion volume fractions below 0.12. At higher inclusion volume fractions, interactions between the inclusions cause the deviations from the theoretical predictions.

Evans [40] considered the inhomogeneous regions of powder particle size or of particle packing results in nonuniform sintering rates. This nonuniformity induces stresses, which in turn create microstructural defects. Evans described a method for computing the transient and residual stresses that accompany differential sintering. He used an elastic-linear viscoelastic analogy to solve the problem. It was shown that the differential shrinkage tends to induce stresses, whereas the viscous flow encourages stress relaxation. The stresses are capable of defect formation in the presence of significant grain boundary diffusion.

Hsueh et al. [41] presented a method for calculating the viscoelastic stresses that develop around heterogeneities during sintering by using constitutive laws derived from

experimental data obtained on partially sintered bodies. Analysis of stresses using literature data for Al_2O_3 reveal that substantial stresses develop only when a slowly sintering heterogeneity is contained within a rapidly sintering host. Furthermore, sintering damage is most likely to occur in this situation. The stresses around heterogeneity vary appreciably with density, particle size and temperature.

DeJonghe et.al.[42] also evaluated the transient stresses within a sintering compact of ZnO containing a uniform dispersion of large inert SiC particles, by mainly utilizing the densification rate data. The dispersion severely limited densification rates by exerting a tensile hydrostatic stress to oppose the sintering pressure of the matrix; this hydrostatic tensile stress increases as the volume fraction of the dispersion increases. The interface stress at the matrix/dispersion boundary increases as the volume fraction of the dispersion decreases. The stresses can attain large values at low volume fraction of the dispersion.

Raj and Bordia [43] analyzed the time-dependent sintering behavior of a bi-modal powder compact, consisting of two regions which sinter at different rates, by applying viscoelastic analysis. The analysis combines both densification and deviatoric creep by assuming two viscoelastic mechanical models to represent the material densification and creep behavior. The maximum tensile stress generated by differential sintering is found to be sensitive to a parameter, β, which is defined as the ratio of the creep rate constant to the densification rate constant. A large value of β reduces the magnitude of the maximum stress, and unless β is large, the densification rate of the composite will deviate significantly from the rule-of-mixture.

The importance of β was also demonstrated by DeJonghe and Rahaman [44]. They proposed that the matrix densification of a particulate composite may be thought of as that of a same single phase material at reduced sintering pressure. The densification rate for the composite can then be determined by the ratio of the creep viscosity over the densification viscosity ($1/\beta$). They found the ratio of creep viscosity to densification

viscosity is of the order of 1 to 10 for crystalline compacts; for glass matrix or liquid-phase sintering ceramic composites, this ratio is expected to be much lower. They determined the ratios of densification rates to creep rates for several different materials. The ratio for crystalline materials is always about one order of magnitude higher than glass materials.

Scherer analyzed the effect of inhomogeneties particularly on glass materials and glass-matrix composites [39,45]. He used a cylindrical model and viscous analogy to calculate the local stress due to small and large pores in the glass powder compact, or rigid inclusion in the glass-matrix composites. The rigid inclusions retard the densification of a sintering body by creating a hydrostatic tensile stress in the glass matrix. He claimed the stress in the inclusion cannot exceed twice the sintering pressure, unless the Poisson's ratio of the glass is negative. Rule of mixture should provide a reasonable approximation to the densification rate if the volume fraction of the inclusions is less than 0.1. This behavior is obeyed by viscous sintering [38] but not solid state sintering [46] in experiments.

Bordia and Scherer [47,48,49] argued that the sintering materials are not linearly viscoelastic, so the Laplace transform technique used in the analysis [40,43] cannot be applied. However, the relevant deformation of the matrix can be treated as purely viscous flow. Therefore, the inapplicability of the viscoelastic analogy becomes unimportant. They compared the constitutive equations in the literature describing the sintering behavior of porous bodies under constraint, and showed that some of them imply a negative Poisson's ratio, which contradicts experimental evidence. They showed that the analyses, which give large values of internal stresses and significant slowdown of the densification, use constitutive laws that underestimate the shear relaxation of the densifying body, and lead to a negative value for the Poisson's ratio. By using the viscous analogy, the Poisson's ratio become positive, but in the mean time the internal

incompatible stresses become theoretically small and cannot account for the substantial slowing down of the densification in the matrix that is observed experimentally. They speculated that the reduction in the densification rate could be a result of subtle interactions between the densifying and coarsening mechanisms in an inhomogeneous powder compact. More experimental data are needed to support their arguments.

2.3.2 Constrained-Film Sintering

The methodology employed in analyzing the sintering of particulate composites are usually applied to the layered composite geometry. Only the sintering of either glass or ceramic films constrained on rigid substrates have been analyzed. Even then, experimental data are very limited, due to the lack of experimental techniques or equipment available to measure the densification kinetics of freestanding films, as well as films constrained on rigid substrates. The available equipment for measuring linear shrinkage profiles, such as the dilatometer [17] and the thermomechanical analyzer (TMA) [18], are best used for samples that are pressed into pellets or disks. Since the sintering kinetics are sensitive to the green microstructure, i.e., density and pore size distribution, pressing a sample into a pellet will produce a sample with different green microstructure than a tape or a film. Hence although numerous theories have been proposed analyzing the effect of sintering films constrained on rigid substrates, few experimental work has yet been done.

Scherer and Garino [50] analyzed the sintering kinetics of a porous glass layer on a rigid substrate. Expressions were derived for the stresses that develop during sintering due to the constraint and for the densification rate of a constrained-film. Garino and Bowen [51] studied the sintering of particle films on rigid substrates experimentally, Silica, zinc oxide, and alumina particulate films were deposited on fused silica, dense alumina and sapphire respectively, and sintered. These represent three different sintering mechanisms, i.e., viscous, liquid-phase and solid-state sintering. They found viscous

sintering will have crack only when tiny, intraparticle pores are presented. No cracking in liquid-phase sintering was found , and the interparticle neck size has to be increased prior to densification to avoid cracking in solid-state sintering.

Bordia and Raj [52] employed viscoelastic analysis to study the sintering behavior of a ceramic film that is constrained by a rigid substrate. They found that the shear rate of the film is more important in the sintering process then its densification rate, when the film is constrained by a substrate. Second, the incompatible stress due to the constraint is time dependent, and reaches its maximum value during the initial stage of sintering. The maximum incompatible stress may be tensile or compressive depending upon the shear response of the material, and if it is tensile, it can lead to the formation of cracks or defects in the ceramic films.

CHAPTER III

EXPERIMENTAL PROCEDURE

3.1   Sample Preparation

The metal used in the experiments was in the form of paste. The metal paste was basically a blend of fine metal powder, organic binder and volatile solvent which was used to form the vehicle and control the viscosity. For our research studies, we used a commercial gold paste from DuPont deNemours Company, which had a solid loading of about 75 volume percent. The initial relative green density of the gold paste was determined to be $42.0 \pm 1.0 \%$, with an average particle size of $2 \mu m$. A SEM micrograph of the microstructure of the gold powder, with the green relative density of $42.0 \pm 1.0 \%$ after removal of organic binder is shown in Figure 3.1. The constrained-film sintering study was carried out on Au, because Au does not have the oxidation-reduction reaction which generally occurs in other metals such as Ag or Cu.

3.1.1   Preparation of Freestanding and Constrained Au Film Samples

The Au film samples were made by screen printing of the commercial gold paste. The details of the screen printing procedure has been given in Chapter II. A photograph of the actual screen printer that was built and used throughout the entire research study is given in Figure 3.2, where Figure 3.2(a) gives the side-view of the apparatus, while the top-view is given by Figure 3.2(b). As shown in the schematic layout of the screen-printing apparatus in Figure 3.3, a vacuum chuck was used to hold the samples into place. Three mechanical dials with 1mil divisions, were used to determine accurate snap-off distances of the screen from the sample, as well as to ensure that the screen was parallel to the sample in order to obtain uniform thicknesses of the screen printed films.
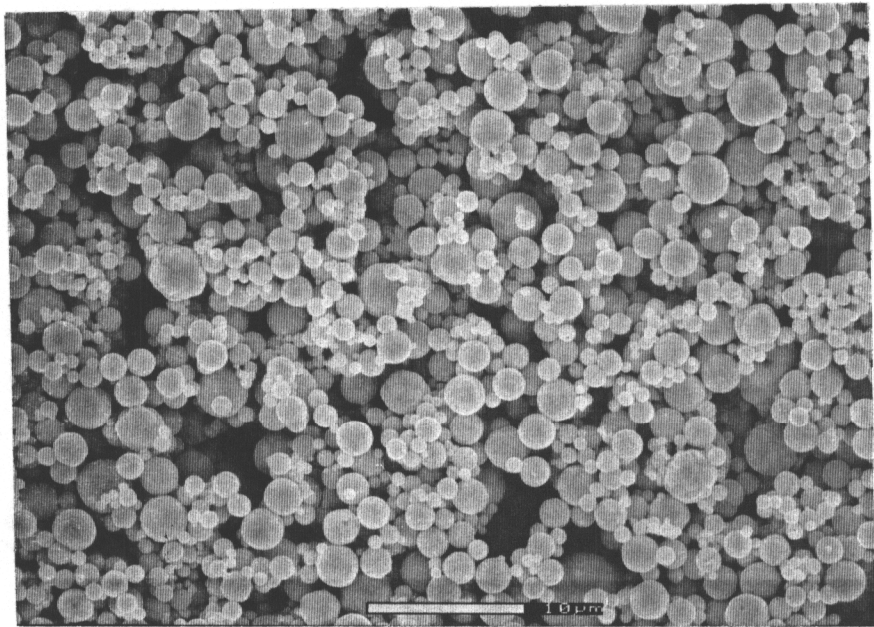
Fig.3.1   Scanning electron micrograph of Au powders heated up to
          450°C and cooled down : relative green density $\overline{\rho} \approx 0.42$.
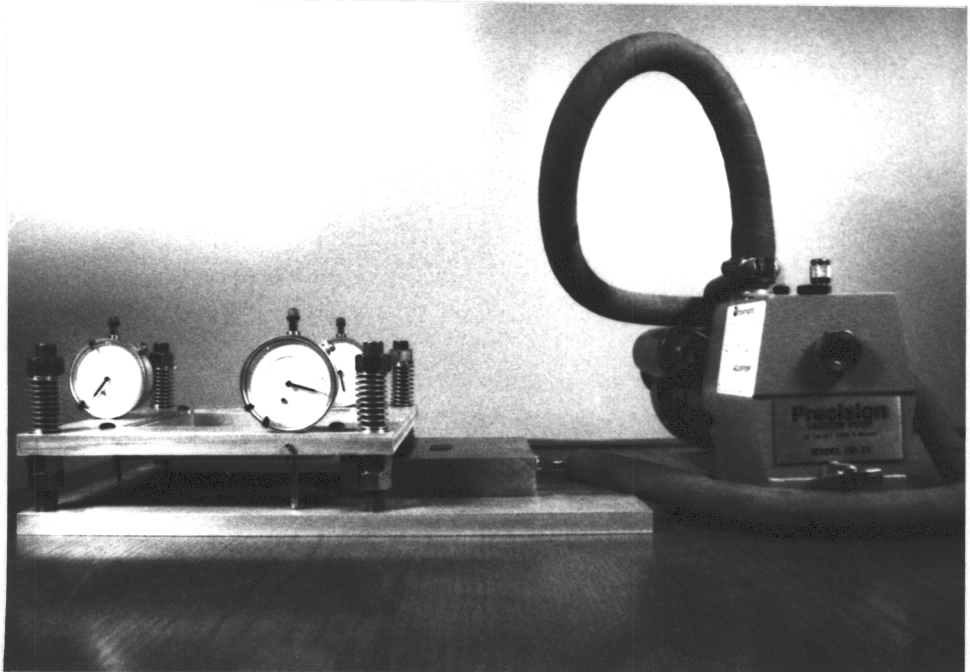
(A)
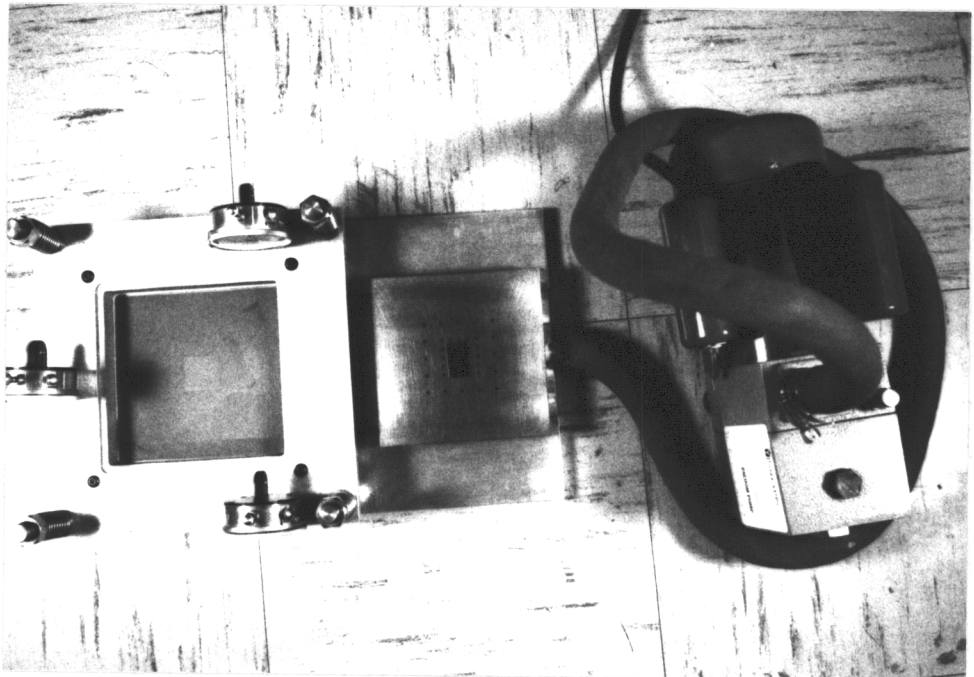
(B)

Fig.3.2   Photographs of the actual screen printing setup used throughout
the study. (A) gives the side-view of the apparatus, while (B)
gives the top-view.

Mechanical Dial

Spring

Bolts

Screen

Vacuum Chuck
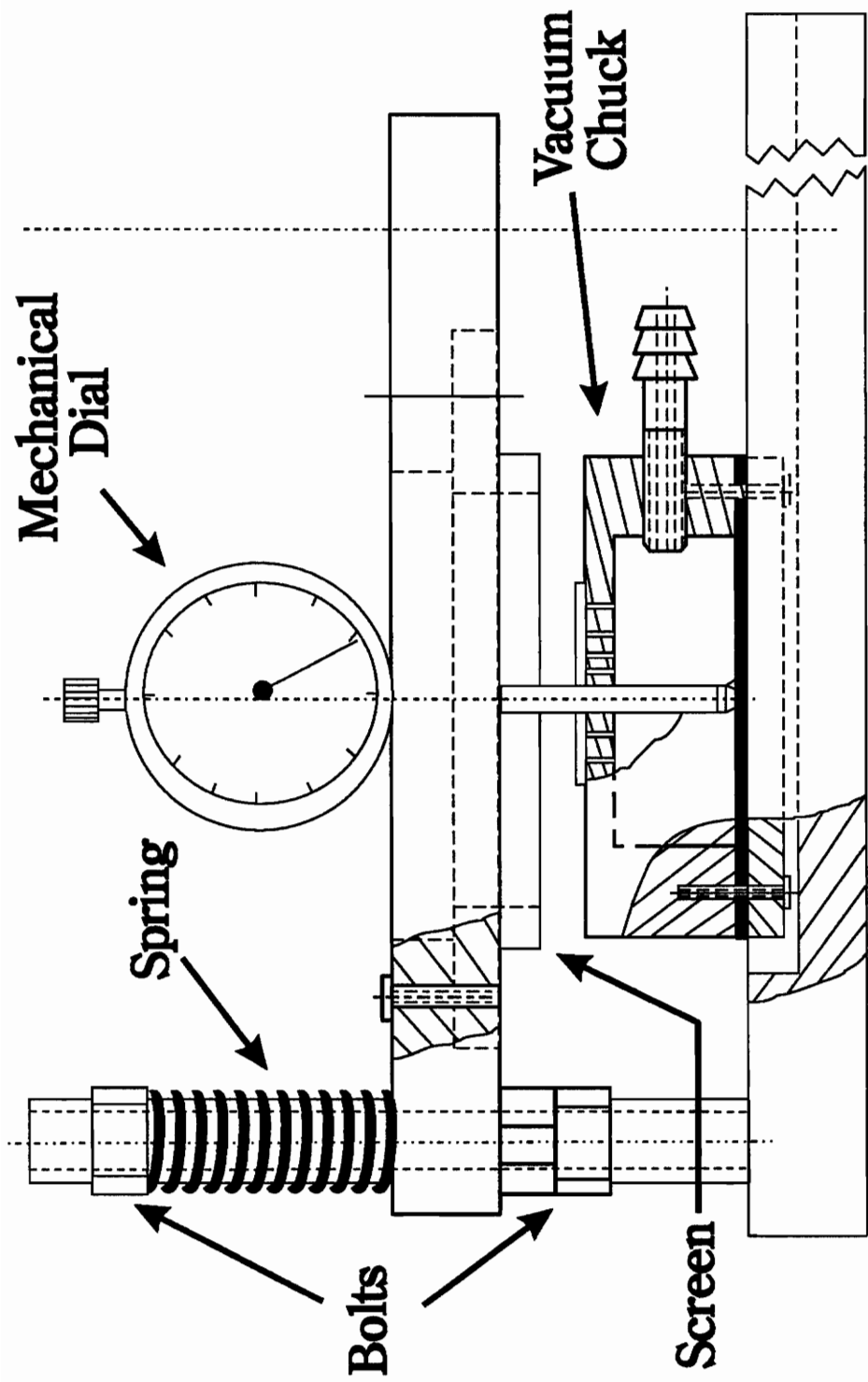
Fig.3.3   A schematic diagram of the actual screen printing equipment used.

The Au paste were screen printed onto well polished and densified alumina substrates. Prior to screen printing, the substrate surfaces were flash-coated by electron - beam evaporation with a 100 $\overset{\circ}{A}$ thick of pure gold film. This surface treatment was found necessary to ensure good adhesion of the screen printed gold film to the substrate during subsequent sintering processes. Film thicknesses of 15μm to 65μm were produced by multiple screen printing with drying after each print. A settle time of 10 minutes was used, after which the samples were then dried for 15 minutes at a temperature of 150°C. The substrates were then broken into small pieces of about 6mm×6mm. All samples were preheated at 450 °C for two hours to remove organic binder, after which the temperature was raised to between 650°C and 900°C at a heating rate of 100°C per minute. The samples were then isothermally sintered at the temperature of study, for a duration of between 30 minutes to 150 minutes.

Out of each gold ink film on the substrate, two samples were made; one freestanding formed by carefully peeling a portion of the film off the substrate, and the remaining one as the constrained sample. The schematic diagram of this preparation process is given in Figure 3.4. This process ensures an identical green density and microstructure in the freestanding film samples with the constrained-film samples, prior to their sintering processes. The mass density of the porous gold films were determined by measuring its thickness with a profilometer, its area under an optical microscope, and its mass after the film was peeled-off the substrate. The relative density of a porous film is defined to be the ratio of its mass density to its theoretical density.

3.1.2   Preparation of Samples for Stress Measurements

The sintering of porous gold films constrained on rigid substrates, results in the development of tensile stresses along the plane of the film. Large enough stresses will produce a curvature in the film constrained on the substrate, depending on the magnitude

SAMPLE PREPARATION

Free Gold Film

Constrained Gold Film

Alumina Substrate

$\updownarrow$ 60 microns

|← 6 mm →|
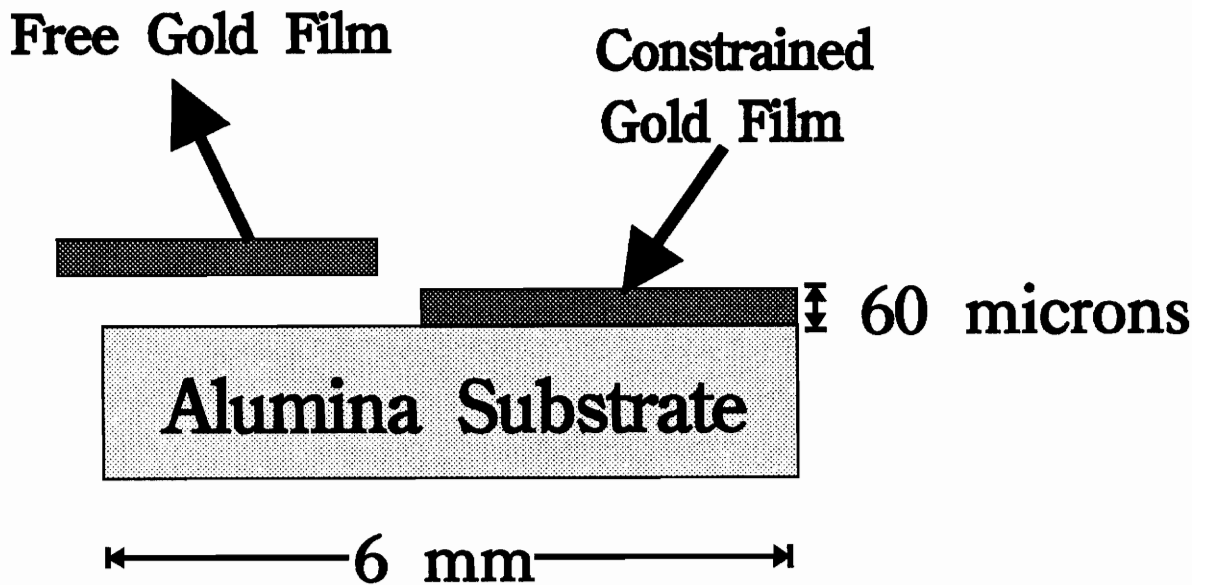
Fig.3.4   A schematic of the sample preparation process that would ensure uniformity between constrained and freestanding samples.

of the stresses developed, as well as the flexibility of the substrate the film is constrained on. Hence in order to observe the development of stresses through curvature measurements, it was necessary to use a substrate with a fairly low Young's modulus. A material with such a low Young's modulus capable of producing a curvature at low stress levels, was determined to be thin silicon wafers. Silicon wafers have a Young's modulus of 130 GPa at room temperature, whereas the Young's modulus of alumina is 365 GPa. One major limitation of the silicon wafer however, was the chemical reaction between gold and silicon at temperatures above 345°C. Since our sintering experiments were carried out at temperatures between 650°C and 850°C, the silicon wafer by itself was not suitable for our experiments. Hence in order to maintain chemical inertness between the gold film and the silicon wafer, a thin buffer layer of amorphous SiO_2 was grown on the surface of the Si wafer.

The same screen printing procedure as described in the earlier section, was employed to produce gold films of 25 μms thick, on 1 mil thick silicon wafers coated with a buffer layer of amorphous SiO_2. The substrate was then sectioned into 4mm×1mm samples, to be used in curvature measurement experiments for the determination of tensile stresses developed during constrained-film sintering. Experiments conducted at temperatures between 650°C and 800°C showed negligible chemical reactions between the gold film and the substrate, but traces of chemical reactions were highly evident at temperatures above 800°C.

3.1.2.1 Amorphous Growth of SiO_2 on Si

A 1 mil thick silicon wafer is placed in a tube furnace which had been heated to and maintained at a temperature of 950°C. Pure oxygen gas that had been bubbled through distilled water, is allowed to flow freely through the tube furnace during the entire growth process. The silicon wafer sits in the tube furnace, flowing with wet oxygen gas

for one hour. After one hour, the silicon wafer is removed from the furnace and allowed to cool in air. A dark bluish coloration is observed for the silicon wafer coated with amorphous SiO_2, where the thickness of the SiO_2 layer is determined to be $700\overset{\circ}{A}$ to $800\overset{\circ}{A}$.

3.2   Experimental Techniques for *in situ* Shrinkage Measurements

There are few experimental techniques available for measuring linear shrinkage profiles of densifying bodies. The available equipment such as the dilatometer or a thermomechanical analyzer (TMA), are best suited for samples that are pressed into pellets or disks. It is well known that sintering kinetics are sensitive to the green microstructure, i.e., the density and the pore size distribution. Hence pressing a sample into a pellet is likely to produce a specimen with green microstructure different from that of a screen printed metal film. Hence, optical setups were constructed to measure the linear shrinkage of freestanding and constrained gold films during isothermal sintering. The densification kinetics of freestanding films are determined by an optical configuration designed to measure width shrinkage profiles, while the optical setup configured for the constrained films, measures the thickness shrinkage profiles of the films. A photograph of the actual optical apparatus that were used throughout the entire length of study, is shown in Figure 3.5.

3.2.1   Apparatus for *in situ* Thickness Shrinkage Measurement

A schematic of the optical system constructed to measure the *in situ* shrinkage profile of the film thickness, of the gold ink film constrained on a rigid substrate is shown in Figure 3.6(a). The optical system uses a low power HeNe laser (4mW), mirrors, lenses, and a position sensitive silicon photo detector. The samples are placed in a compact high temperature furnace, with a temperature controller which is able to maintain the furnace
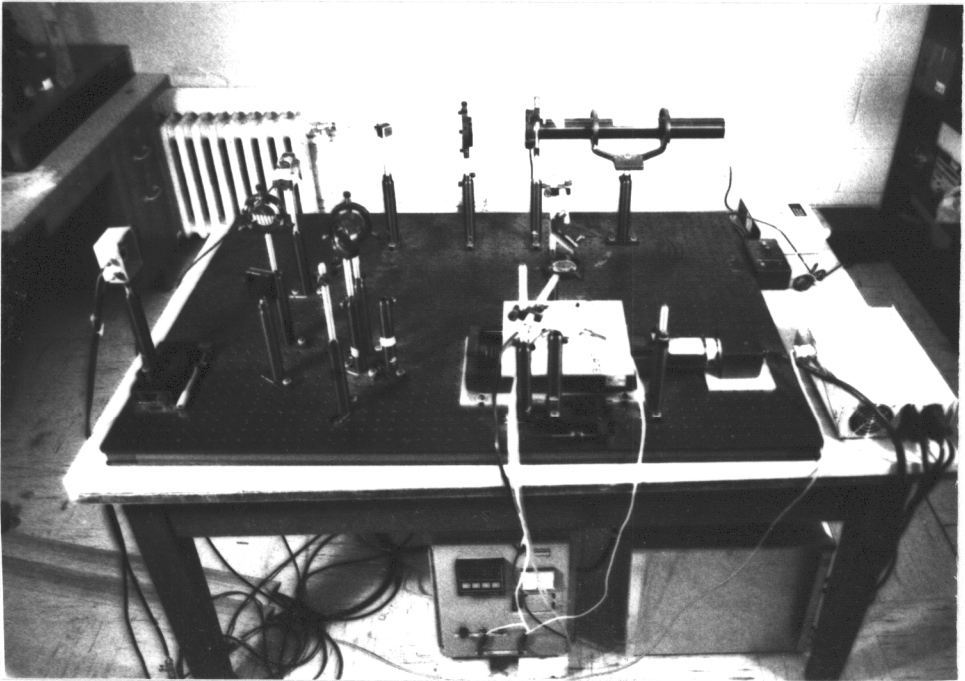
Fig.3.5   A photograph of the actual optical apparatus used during the length of study.
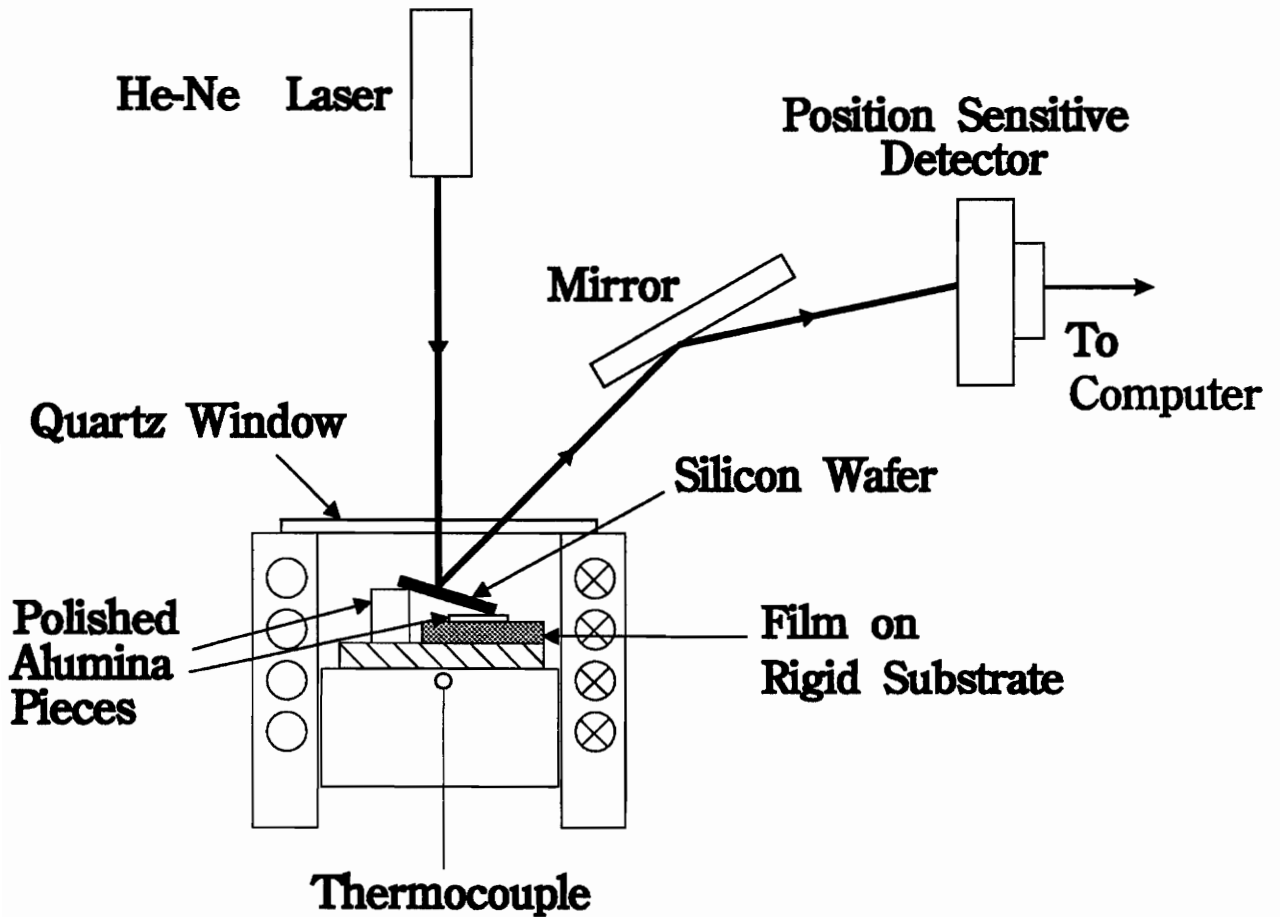
Fig.3.6(a)   A schematic of the optical configuration for *in situ* measurements
of thickness shrinkage profiles of constrained films.
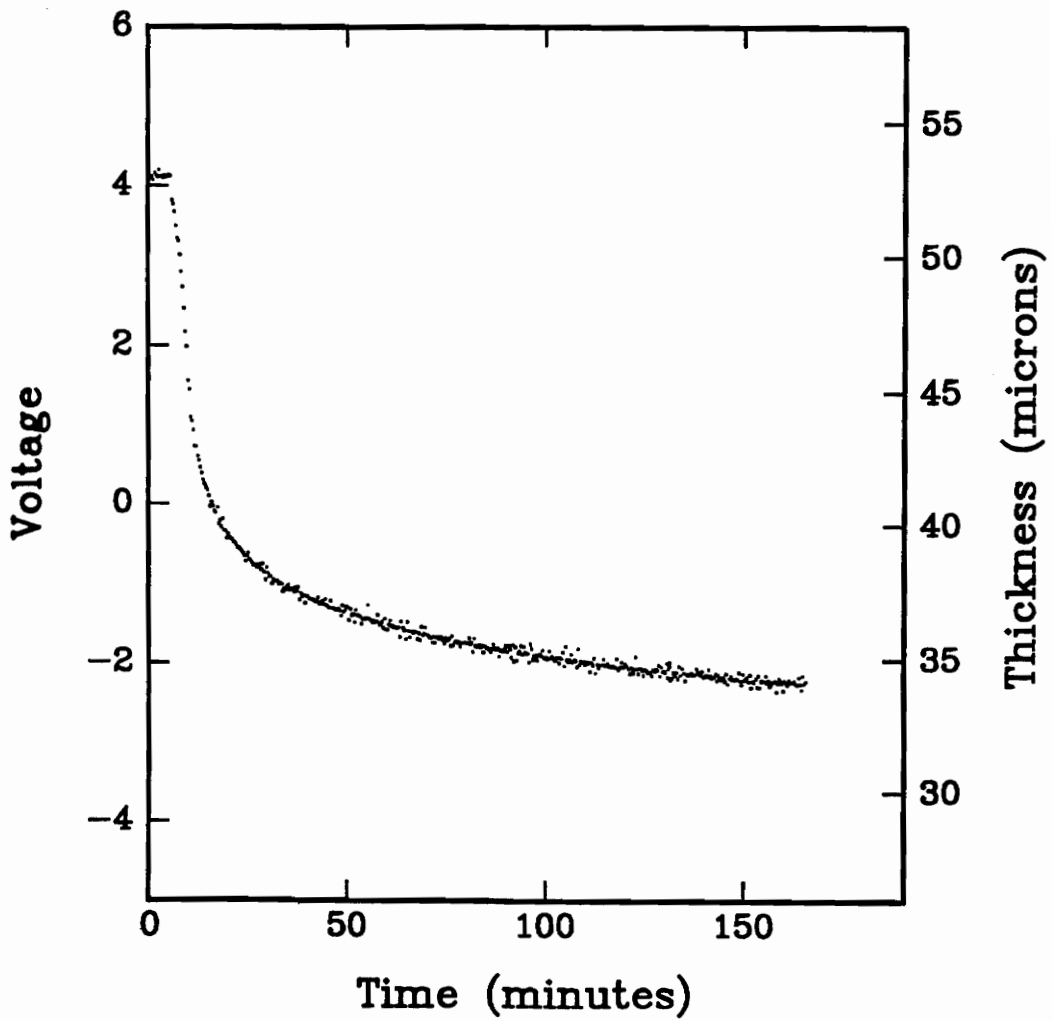
Fig.3.6(b)   Plot of a typical Voltage vs. Sintering time profile obtained during constrained film sintering. The right hand axis gives the corresponding shrinkage in thickness.

temperature profile of within ±2 °C up to 1000 °C. The furnace is capped with a quartz window to ensure isothermal conditions within the furnace, as well as to allow optical access. Acquisition of signals from the photo detectors are done through a personal computer.

Polished and densified alumina pieces are set on top of both the substrate and gold film (refer to Figure 3.6(a)), while the polished silicon piece acting as a reflective medium has its ends resting on the alumina pieces. No reaction was observed between the gold film and the alumina piece resting on it after the sintering process. Very small alumina and silicon pieces were chosen to ensure negligible pressure exerted by the pieces on the gold film due to its weight. During the densification process, the shrinkage in film thickness of the porous gold film would result in a corresponding tilting of the silicon piece. This instantaneous tilting of the silicon reflecting medium with the progressive shrinkage in film thickness during densification, would allow us to measure the shrinkage profile of the film thickness as detected by the position sensitive photo-detector. The thickness of the constrained gold film was determined using a mechanical profiler, both before and after the sintering process. Using linear relationships between the film thickness and the corresponding voltage profile measured, we were hence able to determine *in situ* shrinkage profile of the film thickness during densification. A typical voltage vs. time profile observed during the densification of porous gold film constrained on a rigid substrate is shown in Figure 3.6(b).

3.2.2   Apparatus for *in situ* Linear Width Shrinkage Measurement

A schematic of the scanning system developed to determine *in situ* linear shrinkage profiles of freestanding films during sintering is shown in Figure 3.7(a). The optical portion of the system uses a low power HeNe laser (4mW), mirrors, lenses, and an intensity sensitive silicon photo detector. In addition to the optical portion of the system,
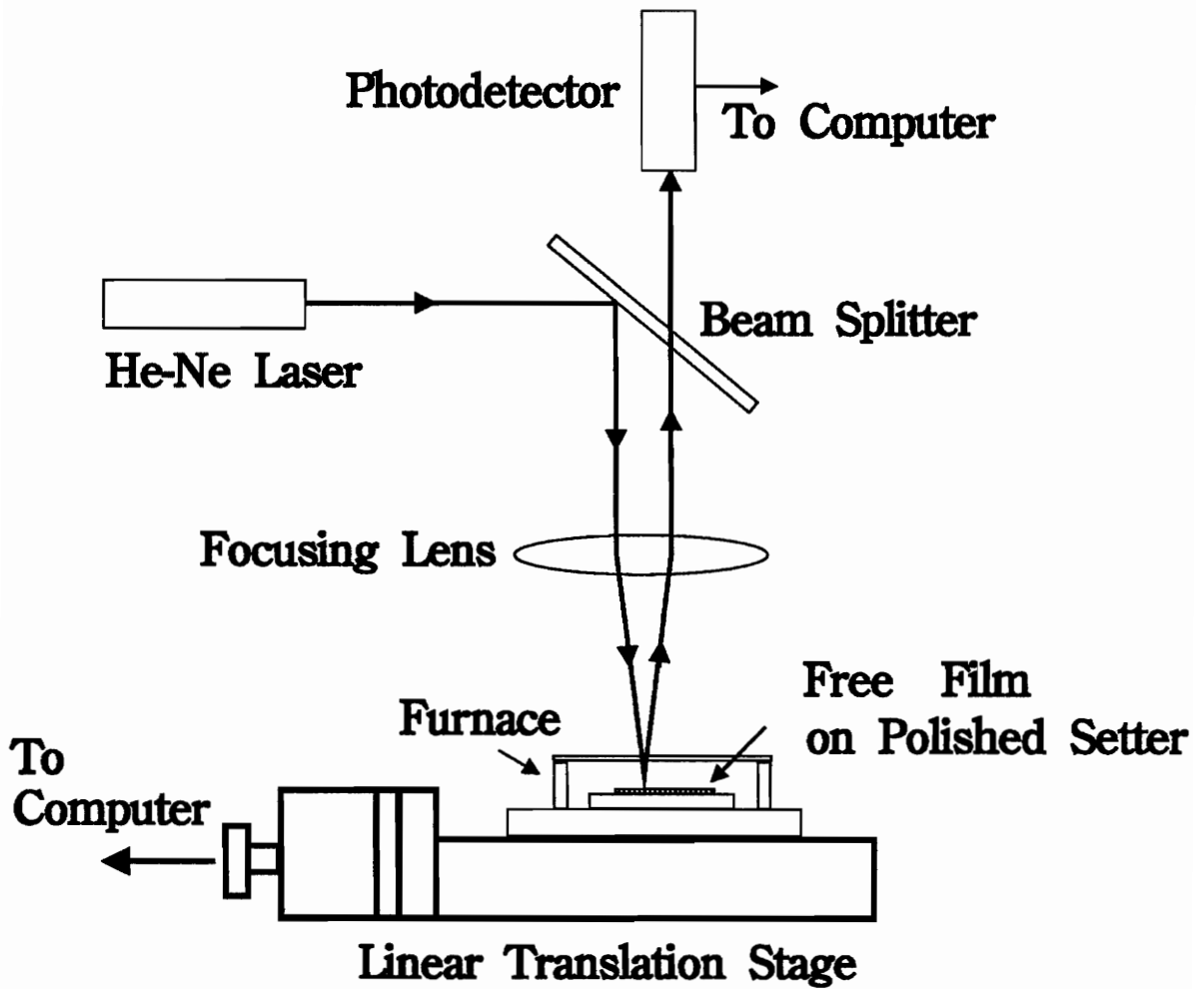
Fig.3.7(a) A schematic of the non-contact optical-scanning equipment for *in situ* measurements of linear shrinkage profiles in freestanding films.
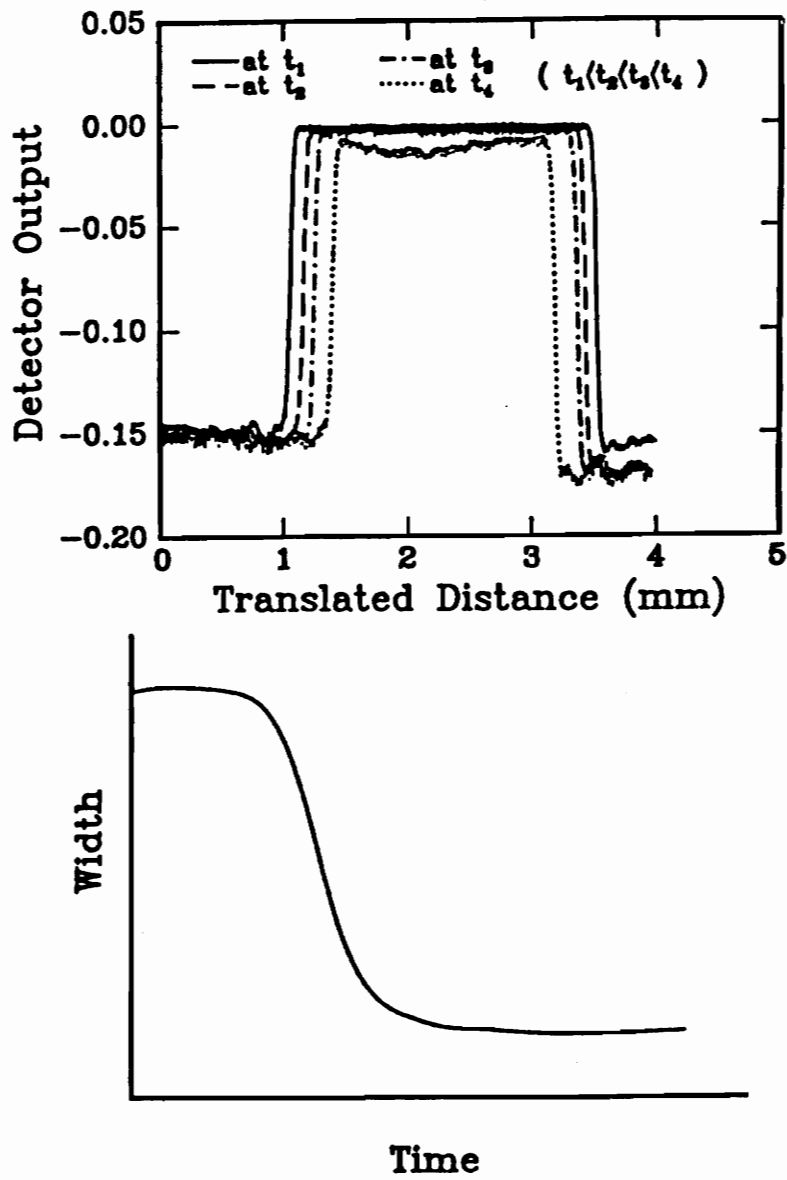
Fig.3.7 (b),(c)   A sequence of detected signals taken at different times
during the sintering process of a freestanding film (B).
The width of the sample shrinks as the sample densifies.
A plot of the Width vs. Sintering time derived from (B), is
shown in (C).

there is also a scanning portion whereby the compact high temperature furnace is attached to a precision linear translation stage. Acquisition of signals from the photo detector and the control of the translation stage, are both done through a personal computer. Samples are sintered freely on top of a fired alumina setter with well polished surfaces. All sintered samples fell easily off the setter.

This technique exploits the contrast between the reflective surface of the setter and the rough surface of the sample to measure the dimensional changes of the sample that occur during sintering. At pre-set time intervals, the scanning of the laser beam across the width of the sample by the movement of the translation stage, allows the dimensional changes to be recorded during sintering. Plotted in Figure 3.7(b) are a series of profiles of the detector signal vs. translation distance obtained at various times during the sintering process. The separation between the half-maxima locations in the output signal corresponds precisely to the width of the samples. The plot of width vs. sintering time profile used in determining the densification profile of freestanding films, is shown in Figure 3.7(c). It is estimated that a minimum linear shrinkage as low as 0.5% can be detected by the technique given the step resolution of the translation stage and the size of the sample.

3.3 Stress Measurement In Constrained-Film Sintering

The determination of internal residual stresses, developed during the deposition of thin films on substrates, through curvature measurements has been well documented in the thin films community [19]. The bending curvature (κ) of the entire structure as a result of in-plane residual stresses in the thinner material is given by Stoney's formula [19] to be

$$\kappa = \frac{6(1-\nu)}{ED^2} \sigma t \qquad (3.1)$$

where D, E, and ν are respectively the thickness, Young's modulus, and elastic Poison's ratio of the thicker material, and σ and t are respectively the residual stress in and thickness of the film material. Hence analogously, we would be able to determine the magnitude of the tensile stresses developed during constrained film sintering, through the measurement of the resulting bending curvature.

3.3.1   Apparatus for Curvature Measurements During Constrained-Film Sintering

A schematic of the optical system constructed to determine the development of curvature due to stresses during sintering of constrained-films is shown in Figure 3.8(a). The optical portion of the system uses a low power HeNe laser (4mW), mirrors, lenses, and a position sensitive silicon photo detector. In this optical system as well, there is a scanning portion whereby the compact high temperature furnace is attached to a precision linear translation stage. Acquisition of signals from the photo detector and the control of the translation stage, are both done through a personal computer.

The samples are placed on a fused quartz glass piece, with the Si / SiO_2 portion of the sample facing upwards. The reflective Si / SiO_2 surface is then able to reflect the incident laser beam, to be detected by a position sensitive photo detector. As the laser scans the sample, any change in the angle of the reflected beam due to the curvature of the sample, would result in the corresponding change in the position of the detected signals. For a completely flat substrate, the angle of the reflected beam remains constant during the scan, hence the position of the detected signal does not change throughout the scan. While in the case of a substrate with a curvature, the changing angle of reflectance would likewise be detected by the changes in the relative position of the signals. A plot of the Relative Detector Position vs. the Relative Substrate Position in Figure 3.8(b), shows that a flat substrate would result in a flat slope, while the slopes of the samples with a
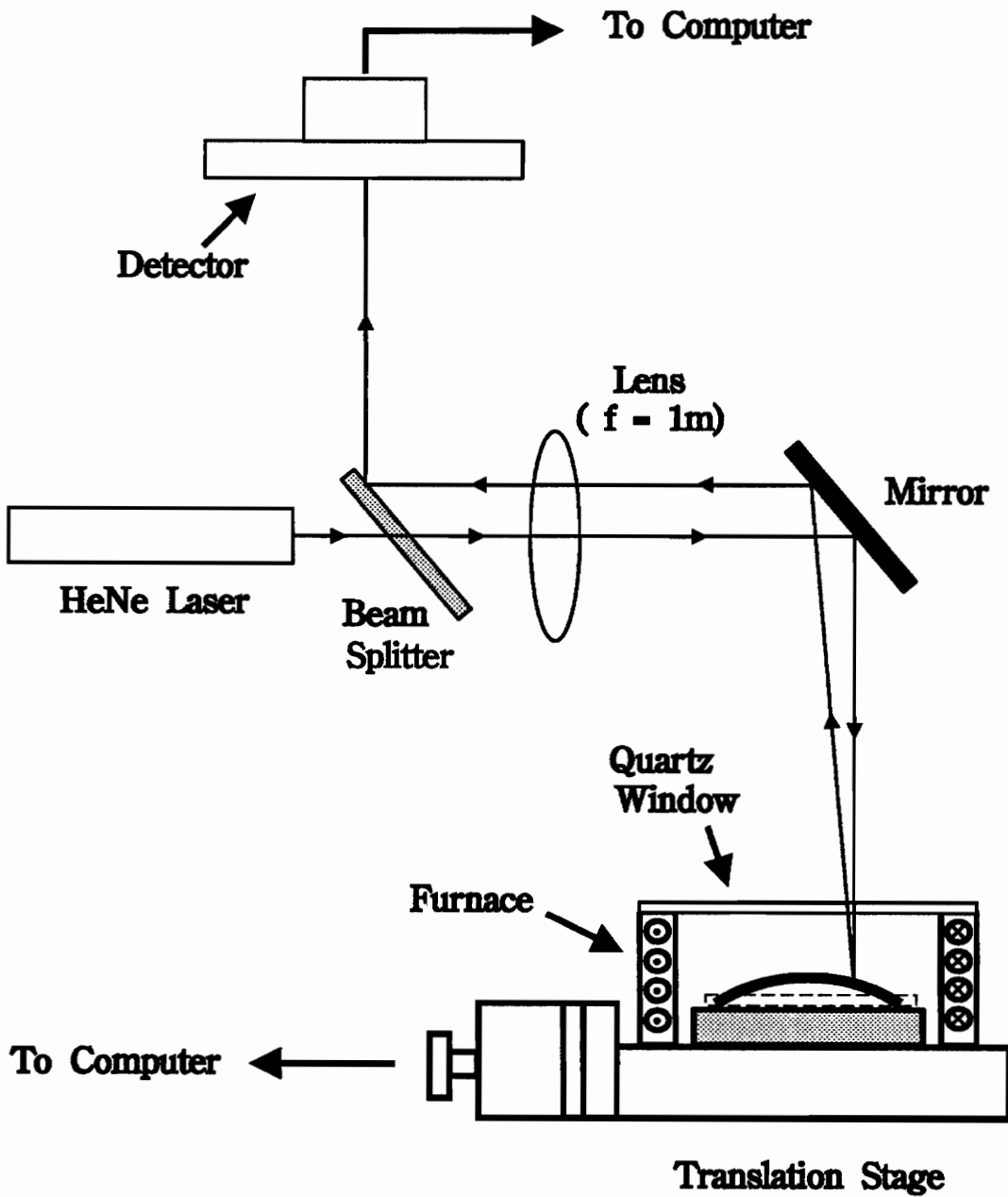
Fig.3.8(a)   A schematic of the optical system for *in situ* measurements of
              curvature developed during constrained sintering of Au films.
              The tensile stresses generated during constrained-film sintering
              are then determined using these curvature measurements.
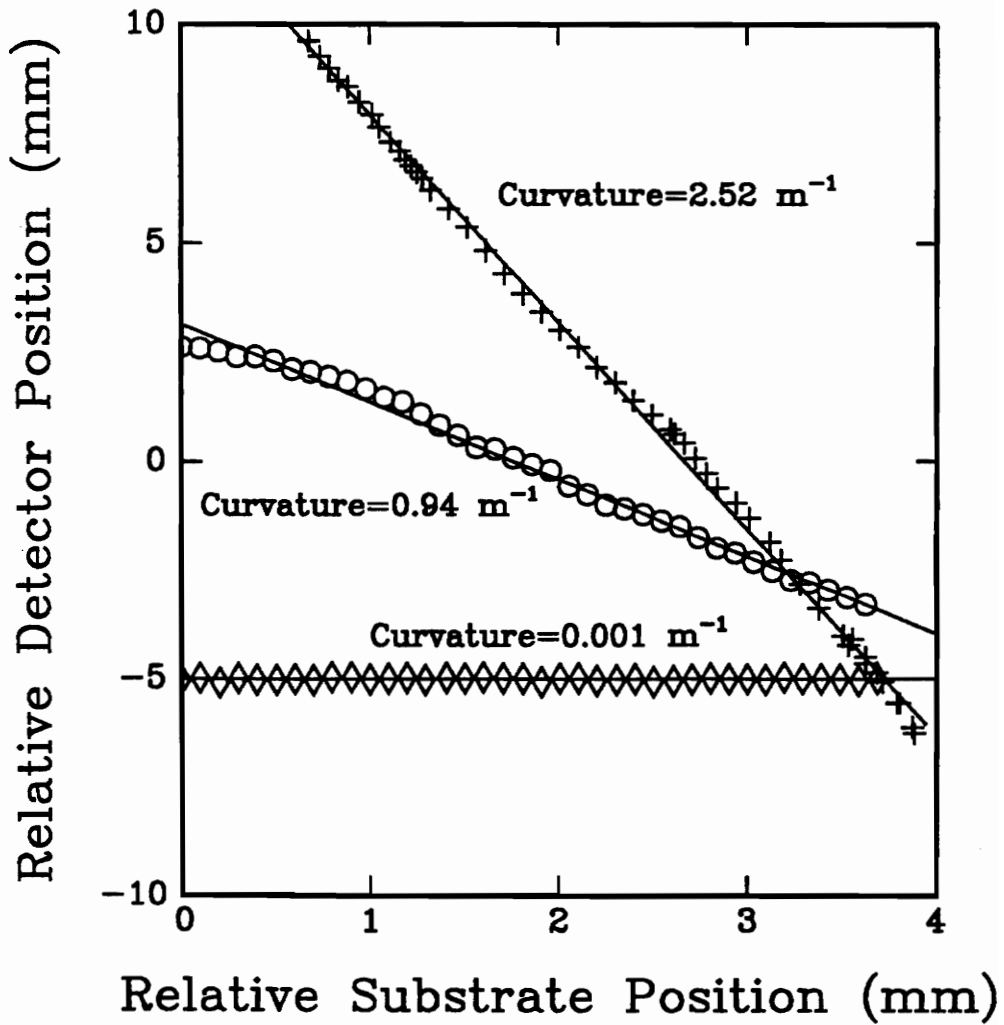
Fig.3.8(b)   A plot of a typical Relative Detector Position vs. Relative
Substrate Position obtained during curvature measurements.
Flatter slopes corresponds to smaller curvature, which then
translates to smaller magnitudes of stress.

curvature are relatively steeper. It should be noted that a higher bending curvature of the sample, would result in steeper slopes observed.

During the sintering process, pre-set scanning intervals allows the changes in the curvature of the samples to be monitored. Hence any relative changes in the curvature of the sample due to stresses developed during constrained-film sintering will be measured. The apparent curvature observed due to the mismatch in the coefficient of thermal expansion between the Si wafer and the SiO_2 layer, was taken into account when determining the curvature obtained due to the stresses developed during constrained-film sintering. It is estimated that this optical system has a curvature detection resolution of 0.01 m^{-1}, given the spot-size of the laser, and the distance between the substrate and the detection plane.

3.3.2 Curvature Calculations from Geometry

The method of calculating the curvature, κ, from a geometrical analysis of the optical configuration will be given. Figure 3.9 gives the geometrical equivalent of the optical configuration of the system. From Figure 3.9, we have

$$\frac{D}{X} = \frac{L - (R/2 - \sqrt{(R/2)^2 - X^2})}{\sqrt{(R/2)^2 - X^2}}$$

(3.2)

For $X \ll R/2$,

$$D \approx \left(\frac{2L}{R}\right) X$$

(3.3)

$(2L/R)$ is the slope of measured D vs. X line.

Therefore

$$\text{Curvature } \kappa \equiv \frac{1}{R} \approx \left(\frac{\text{slope}}{2L}\right)$$

(3.4)

where $L = 0.94$ meter in the optical system.
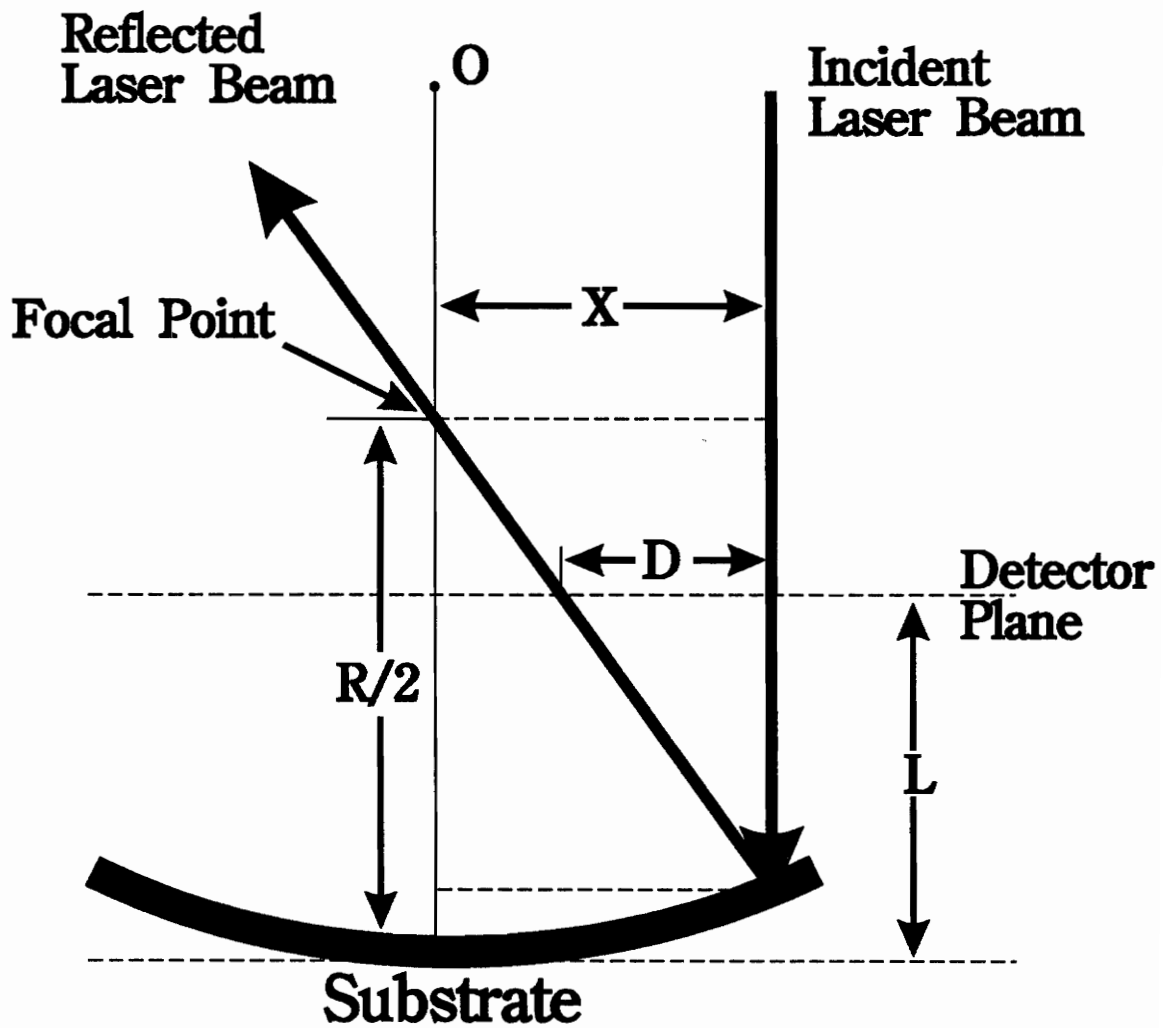
Fig.3.9   A schematic of the geometrical equivalent of the optical
           configuration for calculating curvature values from the slopes in
           Fig.3.8(b).

CHAPTER IV

RESULTS

4.1   Densification Kinetics of Constrained vs. Freestanding Porous Gold Circuit Films.

Using the optical setup as described earlier, we measured the thickness shrinkage and the width shrinkage profiles for the constrained and the freestanding porous gold films respectively. The relative density $\rho(t)$, with respect to the sintering time at the isothermal sintering temperature, was determined by the relations given below.

Constrained Film   : $\rho(t) = \rho_0 \cdot [d_0 / d(t)]$ (4.1)

Freestanding Film   : $\rho(t) = \rho_0 \cdot [w_0 / w(t)]^3$ (4.2)

The relative green density is given by ρ_0. W_0 is the initial width of the free film, while $w(t)$ is the width after a time t at the sintering temperature. D_0 is the initial thickness of the constrained-film, and $d(t)$ is the thickness of the constrained-film after time t at the sintering temperature. In the freestanding film case, the film was assumed to shrink isotropically along the x, y, z directions. This assumption tends to be valid, due to the nearly spherical-shaped gold particles in the paste. During the isothermal sintering of the constrained gold films, no evidence of shrinkage in the x-y plane was observed. Hence densification was only allowed along the direction normal to the plane of the substrate for the constrained-films.

From the above relationships, we were able to determine the densification profiles of freestanding and constrained porous gold films at temperatures of between 650°C and 900°C. Figure 4.1 shows a plot of the relative density vs. time profiles of the constrained and freestanding gold films, subjected to isothermal sintering temperature of 650°C. A
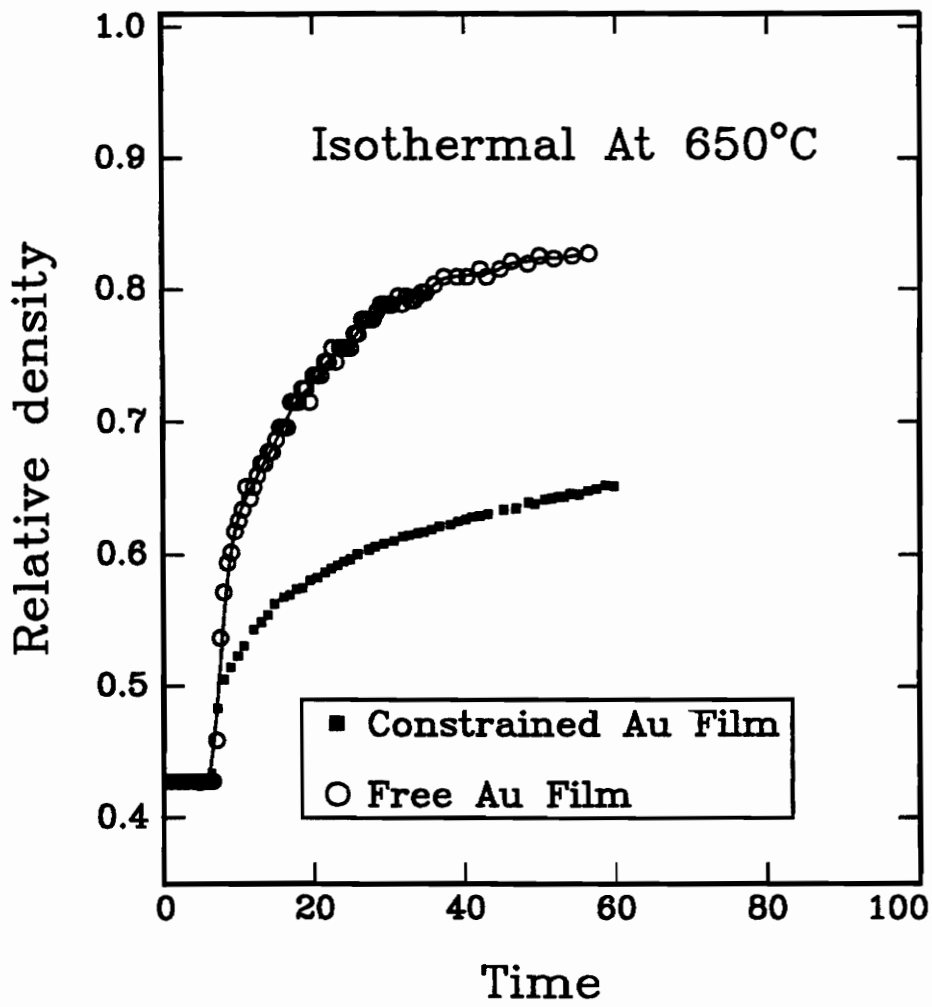
Fig.4.1   The Relative Density vs. Time profile of a constrained and freestanding DuPont Au films, sintered at 650°C
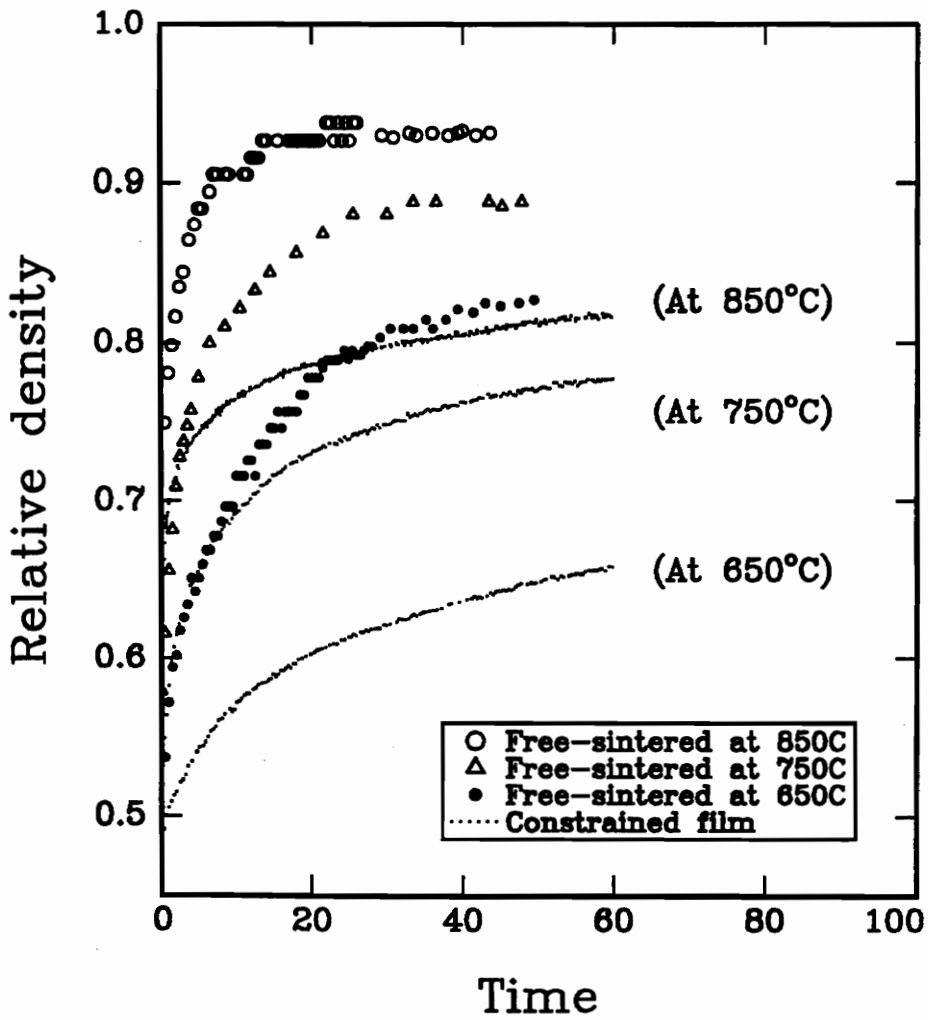
Fig.4.2   A comparison of the densification profiles of the constrained and
           freestanding DuPont Au films at the sintering temperatures of
           650°C, 750°C, and 850°C. Constrained-films have to be
           sintered at higher temperatures in order to be as dense as the free
           films.

comparison of the two profiles clearly shows that the densification rate of the constrained-film is significantly retarded, with respect to the freestanding film. In fact, the densifcation kinetics of the constrained-films were calculated to be retarded by a factor of 10, compared with the densification kinetics of the freestanding gold films. After about 1 hour of isothermal sintering at 650°C, the constrained-film was a lot more porous then the freestanding film : the difference in the final relative densities were determined to be 18±1%. Further experiments conducted at higher sintering temperatures of 750°C and 850°C, also showed significant retardation in the densification kinetics of the constrained-films with respect to the freestanding films. Plotted in Figure 4.2 are the relative density vs. sintering time profiles of freestanding and constrained gold films, sintered at temperatures of 650°C, 750°C and 850°C. For both the constrained and freestanding films, denser gold films were obtained at higher sintering temperatures then at the lower temperatures. However due to the significant retardation in the densification kinetics of the constrained gold films, a much higher sintering temperature was necessary to produce a constrained-film as dense as the free film. A comparison of the microstructure between constrained and freestanding gold films that had been sintered at 650°C for 2.5 hours is shown in Figure 4.3(a). The higher porosity content in the microstructure of the gold films constrained on rigid substrates, gives qualitative support of the results as discussed above. Figure 4.3(b) gives a comparison of the microstructure between the two samples, sintered at a higher temperature of 850°C. In the next section, the experimental results of the tensile stresses developed during the constrained sintering of porous gold films, will be presented.
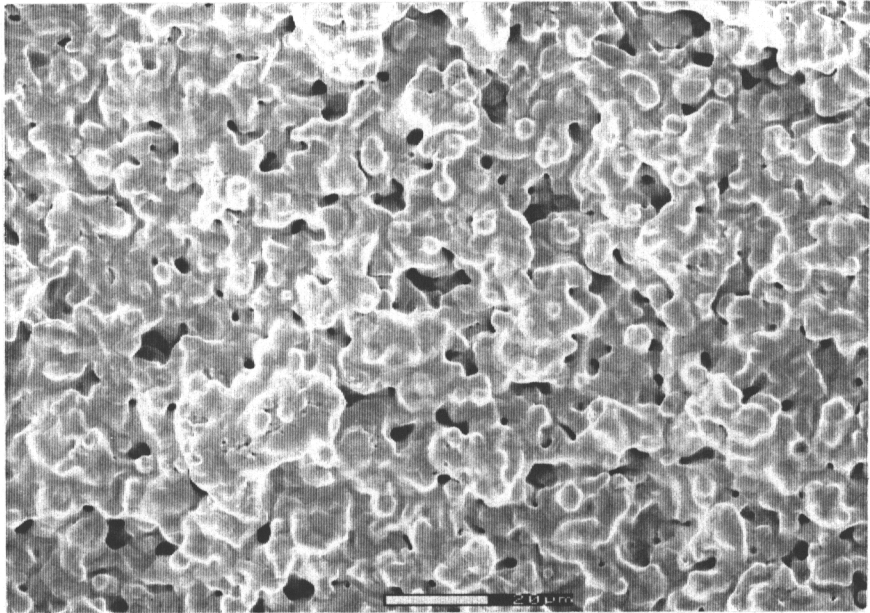
(I)
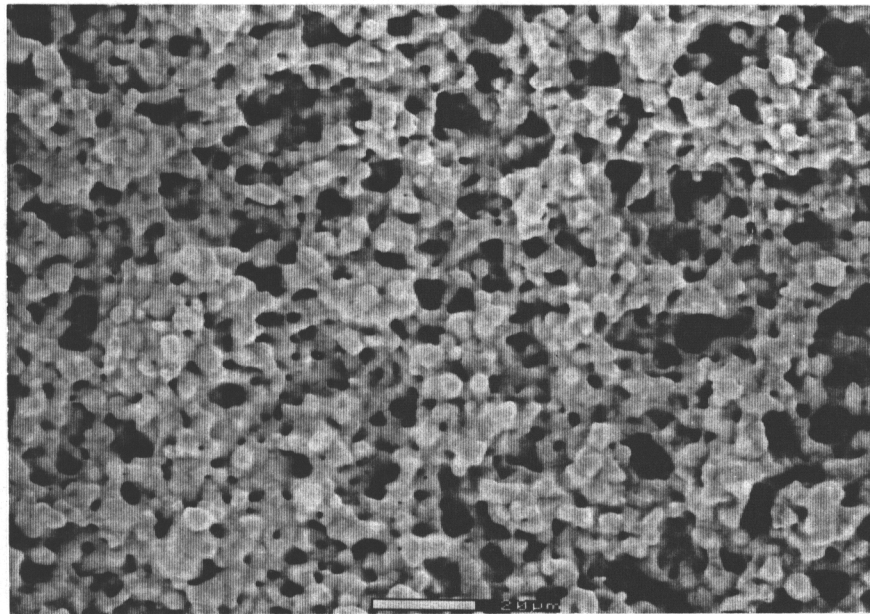
(II)

Fig.4.3(a)   SEM micrographs of the free (I) and constrained (II) DuPont
Au films after 2.5 hr. sintering at $650^{\circ}C$. The constrained-film
has a much higher porosity content than the freestanding film.
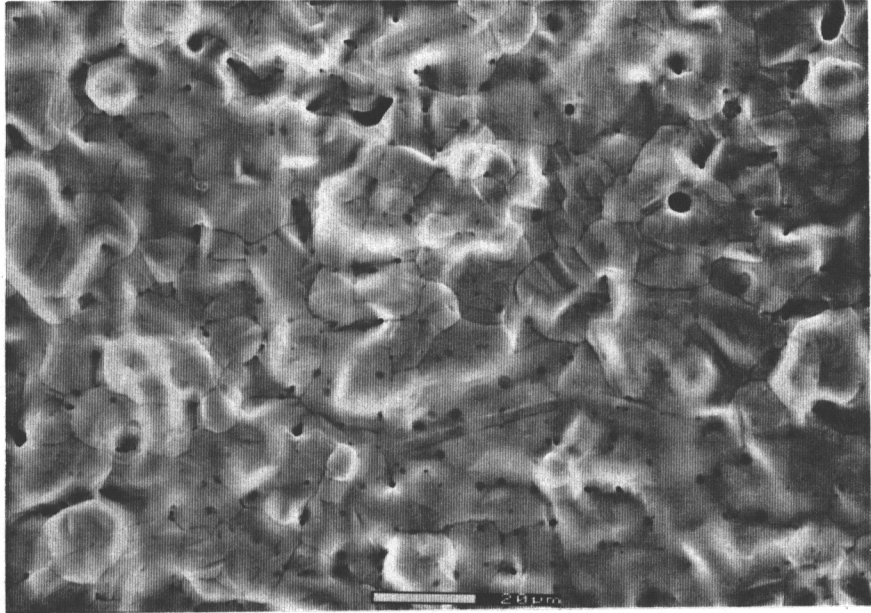
(I)
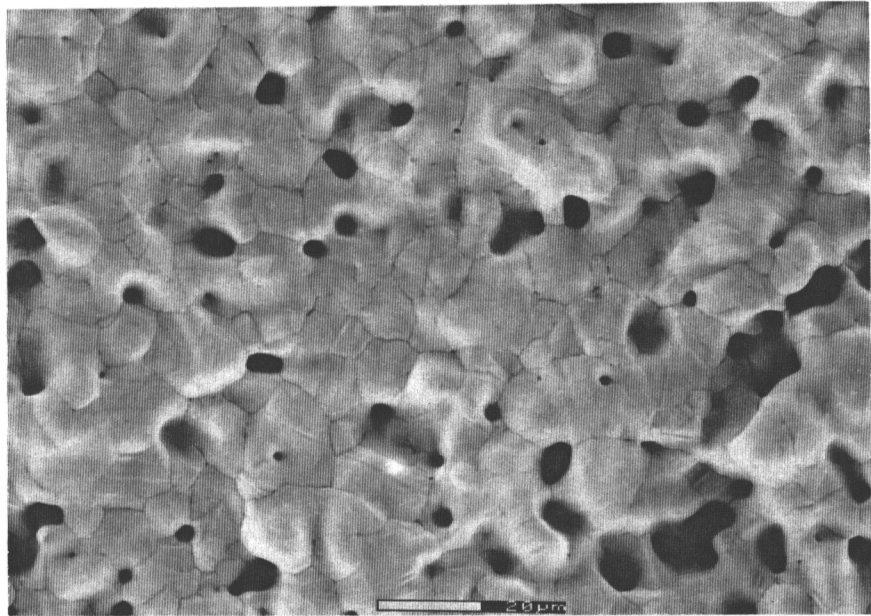
(II)

Fig.4.3(b)   SEM micrographs of the free (I) and constrained (II) DuPont
Au films after 2.5 hr. sintering at 850°C. The constrained-film
again has a higher porosity content than the freestanding film.

4.2   Tensile Stress Measurement During Constrained-Film Sintering

During sintering of a porous gold film constrained on a substrate, shrinkage of the gold film is prevented along the plane of the substrate (in the x-y directions), while densification is only allowed in the direction normal to the substrate (the z-direction). This results in the generation of in-plane tensile stresses within the gold film, due to the constrain placed on the film by the substrate. Although there have been theories put forth by various authors [39,41,43] in trying to determine the magnitude of the internal stresses generated, it is to our best knowledge that no experimental work has been done in actually measuring the stresses, due to the lack of experimental techniques. Using the optical techniques we developed, we have been successful in measuring the tensile stresses generated during the sintering of porous gold films constrained on substrates.

The results of the tensile stress measurements, determined by monitoring the relative change in the curvature of the sample during constrained-film sintering, is shown in Figure 4.4. The tensile stress increased steadily from the onset of ramping from 500°C to 750°C in 3 minutes. A maximum tensile stress of 460 KPa was observed after 5 minutes of isothermal sintering at 750°C, which was then followed by a gradual decline in the stress level with continued sintering time.
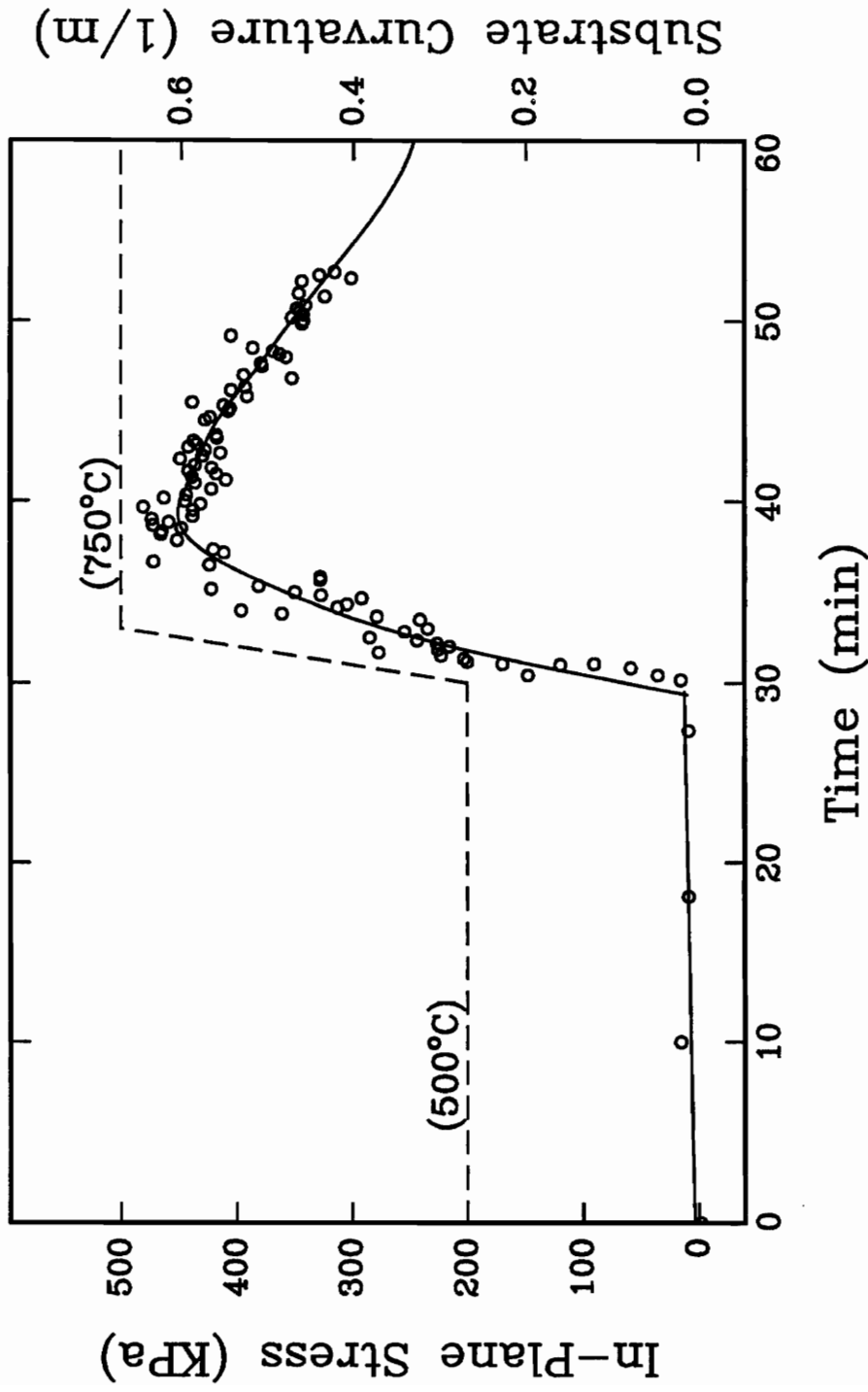
Fig.4.4   Plot of Tensile Stress vs. Sintering time for constrained Au film at 750°C.

Maximum stress obtained = 460 KPa at 5 min. into isothermal sintering temperature.

CHAPTER V.

DISCUSSION

5.1   Introduction

As we reported earlier in the previous chapter, we observed a significant retardation in the densification kinetics of porous gold films constrained on rigid substrates, relative to the densification kinetics of freestanding films. The retardation in the densification kinetics of a sintering body due to inhomogeneous packing of particles [40,45,54], nonsintering rigid inclusions [39,41,43], and attachment to a substrate [51], has been widely observed. Several authors [39,41, & 43] have proposed different reasons for the observed retardation in the densification kinetics of sintering bodies, constrained with rigid inclusions. Raj and Bordia [43], and Hsueh et. al. [41] have developed models assuming the sintering matrix to be viscoelastic, to solve for stresses using the viscoelastic analogy [20,21]. The predicted large viscoelastic stresses were then used to explain the observed retardation effect, by arguing that the large stresses would greatly compromise the driving force for densification.

However, Scherer [39] has shown that the predicted large stresses cannot be valid, as it would then imply a negative Poisson's ratio, which was not observed in the sinter forging experiments. According to Scherer's analyses using a viscous flow model, the predicted stresses are small and hence cannot account for the observed retardation in the densification kinetics.   Instead, Scherer speculates that the interaction between the densifying and coarsening mechanisms in an inhomogeneous powder compact, could be the cause for the retarded densification rate observed.

In the sections to follow, a brief description of the viscoelastic and the viscous flow models will be given. A comparison of the predicted stresses as given by Raj and

Bordia [43], and by Scherer [39], based on the viscoelastic and viscous flow models respectively, will also be given. Our experimental measurements of the tensile stresses measured during constrained-film sintering of porous gold, and the SEM studies on grain growth during constrained-film sintering will be presented. These results will then be used, to suggest the probable factor that might account for the observed retardation in the densification kinetics of porous gold films constrained on rigid substrates during sintering.

5.1.1 Viscoelastic Model

The model presented here follows the same approach that was used for analyzing the sintering behavior of bi-modal powder compacts given by Raj and Bordia [43].

Phenomenologically, the densification behavior of a typical powder compact is shown in Figure 5.1(a). We can simulate the phenomenological densification behavior by using the viscoelastic mechanical model called the Kelvin-Voigt model as shown in Figure 5.1(b). The response of the model to step load p_o, i.e., sintering pressure in this case, is shown in Figure 5.1(c), where Δp is the densification strain. It can be seen that Figure 5.1(c) is similar to Figure 5.1(a) and the spring constant, K_a, the elastic bulk modulus, K_o, and the densification viscosity, η_a, can be defined in the analog. The rate constant for densification, ω_k, is defined as

$$\omega_k = K_o / \eta_a \qquad (5.1)$$

and the time constant for densification , τ, is given by

$$\tau = \eta_a / K_a = (\eta_a / K_o) \cdot (K_o / K_a) = 1 / (\alpha \omega_k) \qquad (5.2)$$

where

$$\alpha = K_a / K_o \qquad (5.3)$$
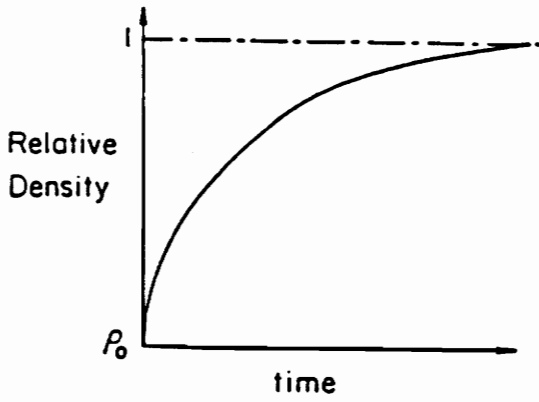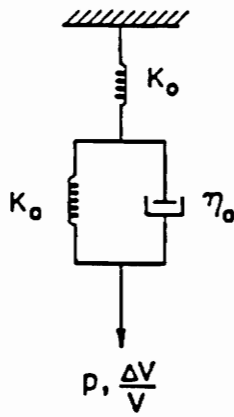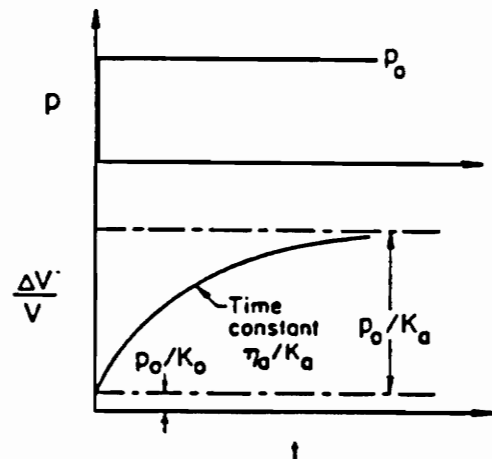
Fig.5.1   (a) Assumed densification response of a porous material; the
phenomenological behavior is approximated by a analog shown in
(b), whose response is illustrated in (c). K_o is the elastic bulk
modulus.   (After Raj and Bordia [43])
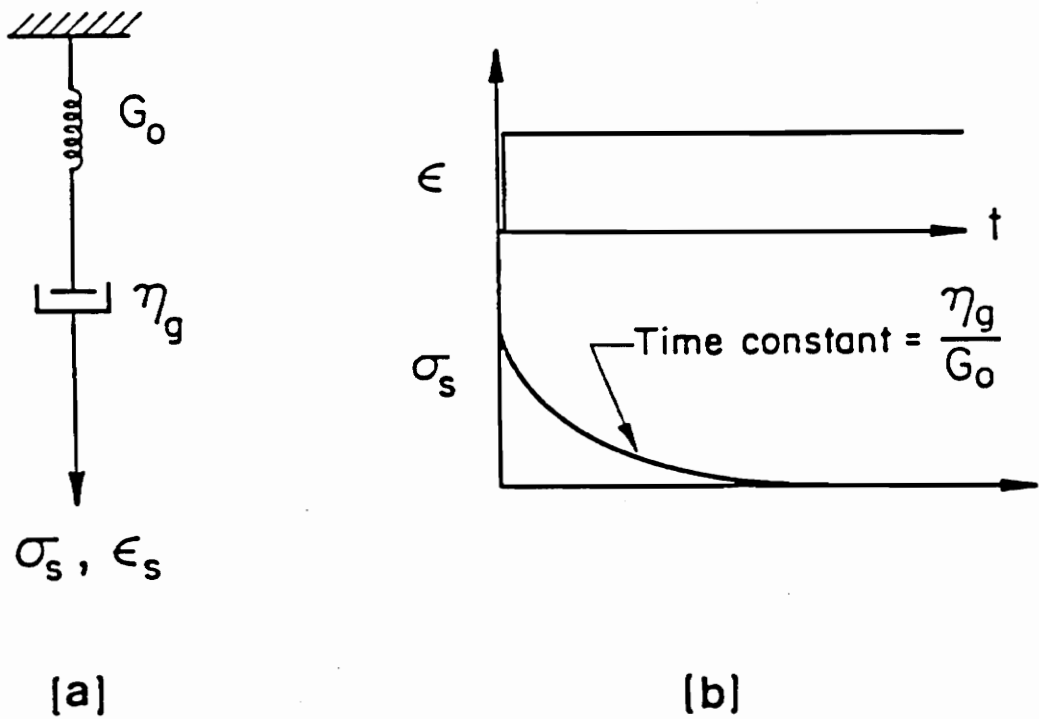
Fig.5.2   (a) Shear relaxation of porous material is approximated by spring
           dash-pot analog. (b) If step strain is applied, stress which would be
           elastic first will gradually relax by shear deformation.
           (After Raj and Bordia [43])

Similarly, the shear response of the material can be simulated by a viscoelastic mechanical model called the Maxwell model, as shown in Figure 5.2(a). The response of the model to a step shear strain is shown in Figure 5.2(b). The shear stress starts from a maximum value and relaxes gradually with time. The rate constant for the shear relaxation, ω_g, is defined as

$$\omega_g = G_o / \eta_g \tag{5.4}$$

where G_o is the shear modulus and η_g is the shear viscosity.

The nondimensional parameter, β, which is called shear relaxation factor is defined as

$$\beta = \omega_g / \omega_k \tag{5.5}$$

i.e., β is the ratio of the intrinsic creep rate to the intrinsic densification rate of the material. The analyses of the sintering bi-modal powder compacts shows that β is an important parameter in the determination of the sign and magnitude of the differential stresses, and hence the defect formation. The physical meaning of β is that β gives a measure of the ability of the material to relax the shear stress. A large value of β is essential to relax the incompatible stresses and prevent the formation of defects.

5.1.2 Viscous Flow Model

The model presented here follows the same approach that was used in analyzing the sintering of a body constrained with rigid inclusions, as given by Scherer [39].

The first step in the analysis involved the choosing of a constitutive equation for the matrix. For an elastic material, the constitutive equation is given by [22]

$$\varepsilon_x = \varepsilon_f + E^{-1}[\sigma_x - \nu(\sigma_y + \sigma_z)] \tag{5.6}$$

where ε_x is the strain in the x direction, ε_f is the free strain, E is Young's modulus, ν is Poisson's ratio, and σ_x, σ_y, and σ_z are the stresses in the x, y, and z directions, respectively. In the viscous analysis of an isotropic porous sintering body, an analogous result of the constitutive equations relating stresses and strain rates are [23]

$$\dot{\varepsilon}_x = \dot{\varepsilon}_f + E_p^{-1}[\sigma_x - \nu_p(\sigma_y + \sigma_z)] \qquad (5.7.1)$$

$$\dot{\varepsilon}_y = \dot{\varepsilon}_f + E_p^{-1}[\sigma_y - \nu_p(\sigma_x + \sigma_z)] \qquad (5.7.2)$$

$$\dot{\varepsilon}_z = \dot{\varepsilon}_f + E_p^{-1}[\sigma_z - \nu_p(\sigma_x + \sigma_y)] \qquad (5.7.3)$$

where $\dot{\varepsilon}_x$, $\dot{\varepsilon}_y$, and $\dot{\varepsilon}_z$; and σ_x, σ_y, and σ_z are the strain rates and principle stresses respectively, while $\dot{\varepsilon}_f$ is the rate of free linear strain due to unconstrained sintering. ν_p is the Poisson's ratio of the porous body. E_p is not a modulus, but a viscosity: it represents the viscous response of the porous material to uniaxial stress, so it will be called the uniaxial viscosity of the porous matrix. As the porosity of the material goes to zero, $E_p \rightarrow 3\eta$ and $\nu_p \rightarrow 1/2$. The elastic response of the sintering body is ignored in the above constitutive equations. The uniaxial viscosity, E_p, and Poisson's ratio, ν_p, of the porous sintering body are related to the shear and bulk viscosities, G_p and K_p, respectively by [47]

$$E_p = \frac{9K_p G_p}{3K_p + G_p} \qquad (5.8)$$

$$\nu_p = \frac{3K_p - 2G_p}{2(3K_p + G_p)} \qquad (5.9)$$

G_p and K_p increases with the bilk density, where $G_p \rightarrow \eta$ and $K_p \rightarrow \infty$ as the porosity goes to zero.

5.1.3 Results of Published Analyses on Stresses : A Comparison of two Models

Raj and Bordia [43] and Scherer [39] have used the viscoelastic and viscous flow models respectively, to predict the generation of internal stresses during sintering of a matrix phase, constrained with rigid inclusions. Although the basic geometry of the problem as given in Figure 5.3 was similar in both analyses, the theoretical calculations predicting the generation of internal stresses was very different. In this section only a brief comparison of the results will be presented, and the reader is referred to the respective papers for a detailed description on the derivation of the results.

For the geometry of the problem as given in Figure 5.3, compressive radial stress, σ_r, and tensile hoop stress, σ_θ, are generated in the matrix during differential sintering. The stresses have their maximum values at the matrix-inclusion interface (i.e. $r = a$) and decreases as $1/r^3$ in the matrix. Let $\sigma_r(a)$ be the radial stress at the interface, and $\sigma_\theta(a)$ be the hoop stress in the matrix interface. The two are related by [43] :

$$\sigma_\theta(a) = -\sigma_r(a)\left[\frac{(1+2v_i)}{2(1-v_i)}\right] \qquad (5.10)$$

where v_i is the volume fraction of the inclusions. The mean (hydrostatic) stress is not a function of r, and is given by [55]

$$\sigma = \frac{[\sigma_r(r)+2\sigma_\theta(r)]}{3} = -\sigma_r(a)\left(\frac{v_i}{1-v_i}\right) \qquad (5.11)$$

In the inclusion, all three stress components are equal to $\sigma_r(a)$. Therefore, the inclusion is under purely hydrostatic stresses, whereas in the matrix both hydrostatic and deviatoric stresses are present.. The uniform tensile hydrostatic stress, σ, has been used to explain the significant retardation of the densification of the matrix as observed experimentally.

Scherer [39] using the viscous flow model, has derived an expression which gave the ratio of $\sigma_r(a)/\Sigma$ in terms of , v_p, the Poisson's ratio, and , v_i, the volume fraction of inclusions. The equation is given below as [39] :
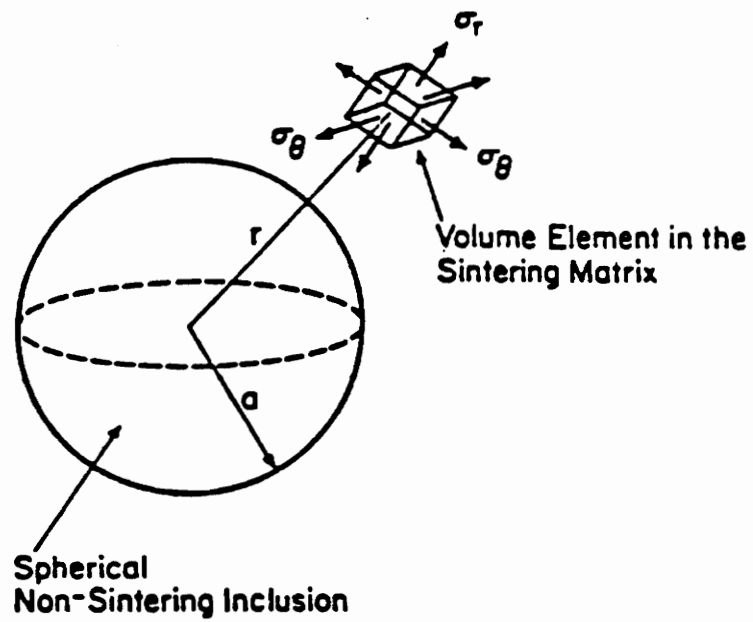
Fig.5.3   Geometry of the problem : a spherical inclusion in a spherical
           shell.   (After Bordia and Scherer [49])

$$\frac{\sigma_r(a)}{\Sigma} = \frac{2(1-2v_p)\cdot(1-v_i)}{(1+v_p)+2v_i(1-2v_p)} \qquad (5.12)$$

where Σ is the sintering potential (driving force for densification). From the above expression, the maximum magnitude of $\sigma_r(a)$ from equation (5.12) is obtained for $v_i = 0$, which means that $\sigma_r(a)$ is less than $|2\Sigma|$ unless $v_p < 0$. Thus, the stresses around a rigid inclusion in a sintering matrix have upper bounds such that $|\sigma_r(a)| < |2\Sigma|$ unless $v_p < 0$. A negative Poisson's ratio was never observed experimentally.

On the other hand, Raj and Bordia[43] have predicted large stresses using the viscoelastic model, as given in the expression below :

$$\left[\frac{\sigma_r(a)}{\Sigma}\right]_{max.} = \frac{4(1-v_i)}{4v_i+9\beta} \qquad (5.13)$$

where the variables are the same as the above, and β is the shear relaxation factor as described in an earlier section. It can be seen that large interfacial stresses are predicted for small values of v_i and β. $\beta \ll 1$ implies that creep relaxation is insignificant relative to densification and conversely for $\beta \gg 1$. For the value of $\beta = 0.01$, the calculated value of the maximal radial stress around the rigid inclusions was $|\sigma_r(a)| < |45\Sigma|$. It was also shown that the hydrostatic tensile stress, σ, generated in the matrix was of the same order as the sintering potential, Σ, for small values of β. This would explain the significant retardation in the densification rate of the matrix, even for small volume fraction of inclusions.

Hence, small values of the radial stress, $|\sigma_r(a)| < |2\Sigma|$, were predicted by Scherer [39] using the viscous model analogy. The hydrostatic tensile stress, σ, would then equal 2-22% of Σ, for volume fraction of inclusions of between 1% to 10%. This small

hydrostatic tensile stress, σ, would be insufficient to account for the retardation in the densification kinetics of a sintering matrix constrained by rigid inclusions. On the other hand, the viscoelastic model which predicted a large hydrostatic tensile stress, σ, equal to 60-90% of Σ, would be able to compromise most of the driving force for densification, and hence would explain the observed retardation in the densification kinetics of the sintering matrix.

In the next section, we will use our experimentally measured in-plane tensile stress, σ, developed during constrained-film sintering, and compare it with the stress values predicted by the two models. This would enable us to have a better understanding of the role of the in-plane tensile stress, on the observed retardation in the densification kinetics during constrained sintering of porous gold films.

5.2 Role of Stresses in the Densification Kinetics of Constrained-Film Sintering

The main driving force for the densification of a crystalline body, is given by the mean pressure [52],

$$p = -\frac{\sigma_x + \sigma_y + \sigma_z}{3} \tag{5.14}$$

where σ_x, σ_y, and σ_z are the principle stress components. In the sintering of the freestanding film case, $\sigma_x = \sigma_y = \sigma_z = -\Sigma$, where Σ is the sintering pressure given by

$$\Sigma = \frac{2\gamma_s}{r} \tag{5.15}$$

Hence the driving force for the densification of freestanding gold films, would be $p = \Sigma = (2\gamma_s/r)$, where γ_s is the surface energy, and r is the radius of curvature of the pores. Note that the average surface free energy of gold is taken to be $\gamma_s = 1.39 \ \text{J} \cdot \text{m}^{-2}$, and the

measured radius of curvature on the average was $r \cong 2.0 \mu m$, then from equation (5.15), p $= \Sigma \cong 1.39\,MPa$.

In the case of a porous gold film constrained on a rigid substrate, the porous film is constrained from densifying along the x and y direction. This would result in the development of tensile stresses, σ, along the plane of the substrate, hence altering the values of σ_x and σ_y. Since there is no constraint along the plane normal to the substrate, the porous film is allowed to densify freely along the z-direction. Hence in the constrained-film case, $\sigma_z = -\Sigma$, but $\sigma_x = \sigma_y = \sigma - \Sigma$. Substituting these relations into equation (5.14), we obtain the driving force for the densification of porous films constrained on rigid substrates to be,

$$p = \Sigma - \frac{2}{3}\sigma \qquad (5.16)$$

From the above equation, we can clearly see that a large stress, σ, would retard the densification rate by compromising much of the driving force for densification.

In our experimental measurements of the in-plane tensile stresses generated during constrained film sintering, we have determined the maximum tensile stress, σ, to be 460 KPa. From equation (5.16), the effective stress that would compromise the sintering pressure would be equal to about 22% of Σ. Although this magnitude of stress is large enough to produce camber during co-sintering of multilayer structures, the measured hydrostatic tensile stress is considered to be too small to account for the factor of 10 times the observed retardation in the densification kinetics of the constrained-films, compared with the densification kinetics of the freestanding films during sintering. This was also predicted by Scherer[39] using the viscous flow model, where Scherer determined the magnitude of the internal hydrostatic tensile stress to be too small to account for the observed retardation in the densification kinetics of constrained sintering bodies. Hence

from our experimental measurements of the tensile stresses, we can conclude that the main cause for the observed retardation in the densification kinetics of the constrained-films, is not due to the in-plane tensile stresses.

5.3   Role of Grain Growth During Constrained-Film Sintering

A competing process for the densification kinetics during sintering of a porous crystalline body, is the coarsening of the grains (grain growth) during sintering. As the grains grow during the sintering process, it consequently loses its curvature and hence the sintering potential for densification decreases. The growth of grains also causes the pores between the grains to grow smaller and smaller. The pores eventually loses connectivity with the other pores and becomes trapped in the microstructure. Although the decrease in the sintering potential with increasing density may at first appear to be unusual since the pores should become smaller and their curvature, and therefore the sintering pressure, should increase with decreasing porosity. That would certainly be the case if the number density of the pores remained constant. However with grain growth, the number of pores decreases rapidly with densification such as to reduce the overall sintering potential.

A general equation relating the sintering rate to the grain size for a crystalline material is given by [24],

$$\dot{\rho} = \frac{A}{d^n} \cdot \frac{\gamma V^{2/3}}{RT} \cdot \exp(-\frac{Q}{RT}) \cdot f(\rho) \qquad (5.17)$$

where $\dot{\rho} = (\frac{d\rho}{dt})$, is the instantaneous rate of densification, A is a constant independent of the other variables, d is the grain size, V is the molar volume, γ is the surface energy, T is the absolute temperature, Q is the activation energy, R is the gas constant. n = 4 if the dominant diffusion mechanism is by grain-boundary diffusion during the sintering process,

and n = 3 if diffusion takes place through lattice diffusion. $f(\rho)$ is a function of density, and is given in reference [36] to be :

$$f(\rho) = \frac{\rho}{\ln\left(\frac{1}{1-\rho}\right) - \frac{1}{2}\rho(\rho+2)} \qquad (5.18)$$

where ρ is the relative density. From the above function of relative density, we see that a higher ρ would result in a lower, $f(\rho)$, and hence a lower densification rate according to equation (5.17).

The densification rate is highly dependent on grain growth, especially if the dominant diffusion mechanism during the sintering process is by grain-boundary diffusion. A high grain growth rate would result in a significant reduction in the densification rate during sintering. An increase in grain size by a factor of two, reduces the densification rate by a factor of eight, if it is lattice diffusion controlled, or by sixteen, if it is grain boundary diffusion controlled. Hence it is probable that the observed retardation in the densification kinetics of porous gold films constrained on rigid substrates, is due to a higher grain growth rate in the constrained-films relative to the grain growth rate in the freestanding films. If this was the case, the constrained-films would have a microstructure whose grain size are much higher than the grains in the free films, after being subjected to identical sintering conditions for both samples. In fact, our calculations have shown that in order to account for the retarded densification rates observed in the constrained-film samples, the grain size in the constrained-film samples have to be at least 5 times larger than the grain size of the free film samples. In our SEM studies on the grain size of the constrained-film samples and the free films samples, we observed that the grain size difference between the two samples were negligible. Figure 5.4(a) shows the SEM micrographs of the constrained-film samples and the free film samples of gold, that had

been sintered at 850°C for 2.5 hours under identical sintering conditions. A qualitative as well as a quantitative analysis of the grain size of both samples, revealed that both had a grain size in the range of 5.5 - 8 µms. Figure 5.4(b) shows the SEM micrographs which gives a qualitative comparison of the grain size of the constrained-films and the free films, that were sintered for 2.5 hours at a lower temperature of 650°C.

Hence from our SEM studies of grain size comparison between sintered constrained and freestanding films, we did not observe a significant difference in the grain size between the two samples. Thus we are able to conclude that the negligible difference in grain size between the constrained and free film samples, cannot properly account for the retarded densification kinetics observed during sintering of the porous gold films constrained on rigid substrates.
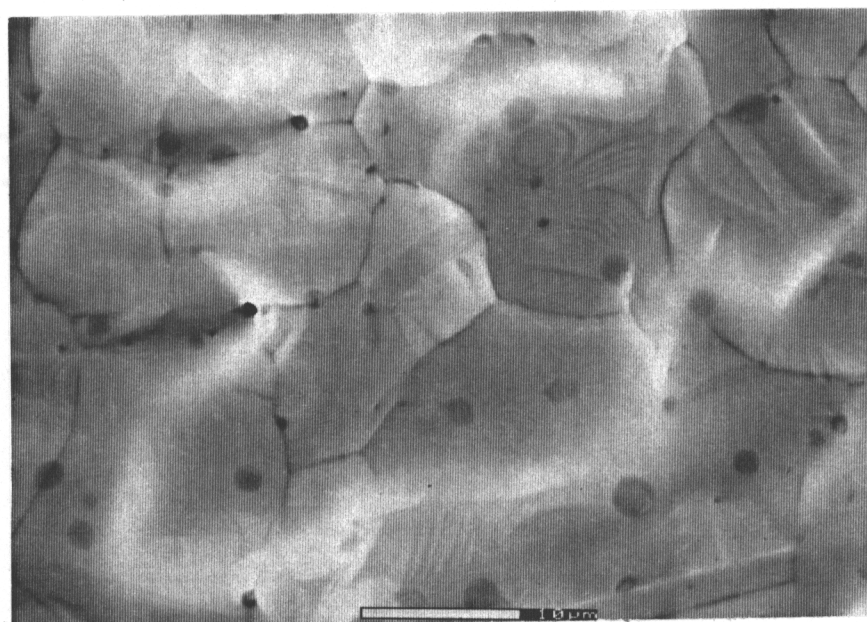
(I)
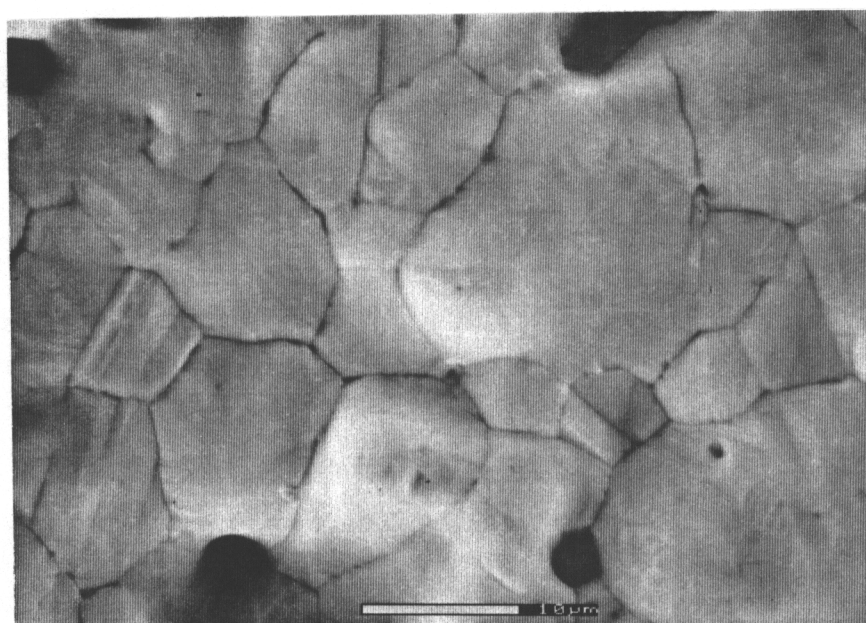
(II)

Fig.5.4(a) SEM micrographs of the free (I) and constrained (II) DuPont Au films after 2.5 hr. of sintering at 850°C. No significant difference in grain size was observed between the two samples.
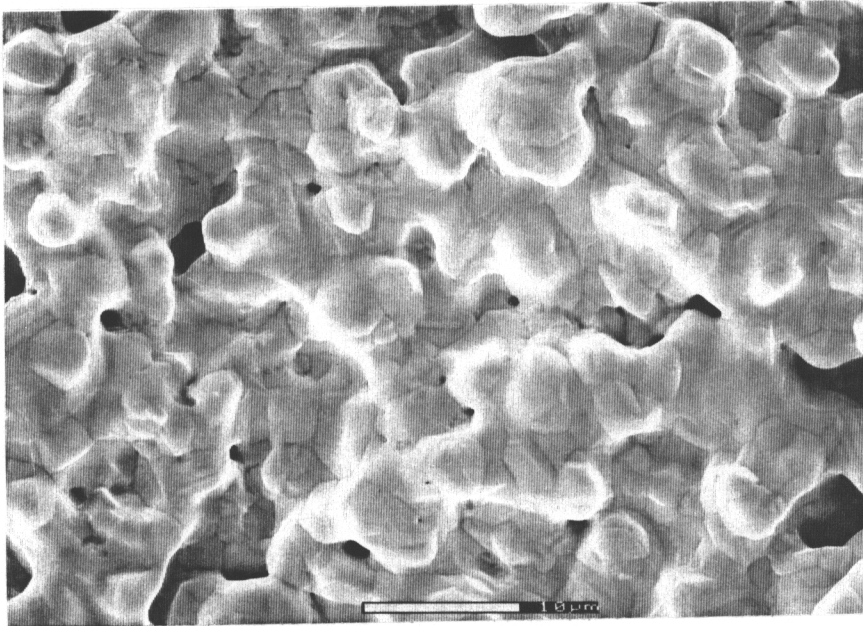
(I)
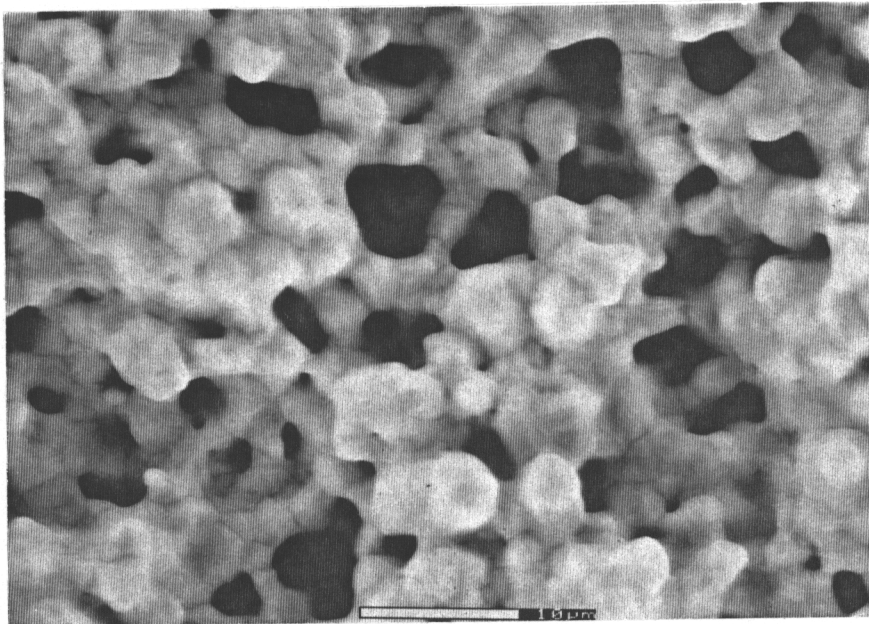
(II)

Fig.5.4(b)   SEM micrographs of the free (I) and constrained (II) DuPont Au films after 2.5 hr. of sintering at 650°C. Again, no significant difference in grain size was observed between the two samples.

5.4   Probable Causes for the Observed Retardation in the Densification Kinetics During Constrained-Film Sintering.

In our analysis of trying to determine the cause/causes for the observed retardation in the densification kinetics during sintering of constrained-films, the effect of grain growth and the effect of internal stresses were ruled out based on our experimental results. However, another possible explanation for the observed retardation in the densification kinetics, might be due to different diffusion mechanisms that are dominant during the sintering of the constrained and the freestanding films. In the sections to follow, an analysis of our results on the densification profiles for the constrained and freestanding films will be presented in an attempt to explain the above phenomenon.

5.4.1   Determination of Activation Energies for Densification in Constrained vs. Freestanding Films.

In order to calculate the activation energies for the densification of the constrained and freestanding porous gold films, we took an Arhenius plot of $(\dot{\rho} T)$ vs. $(1/T)$. The plots of $(\dot{\rho} T)$ vs. $(1/T)$ of gold films for relative densities ranging from 0.63 to 0.70 for the constrained-films, and the relative densities ranging from 0.7 and 0.75 for the freestanding films, are shown in Figure 5.5. It can be seen from Figure 5.5 that the sets of data obtained for the constrained and freestanding gold films, gave a fairly constant value of activation energies for the two cases.

A point of concern was to ensure that the densification rates observed at a particular relative density, was only dependent on the isothermal sintering temperature and not due to a difference in the microstructure. During the sintering process, a relative density of 0.75 would be reached only after a short sintering time at a higher sintering temperature of $850^{\circ}C$, but a longer sintering time would be required at a lower sintering temperature of $650^{\circ}C$, to reach the same relative density. It was hence crucial to ensure
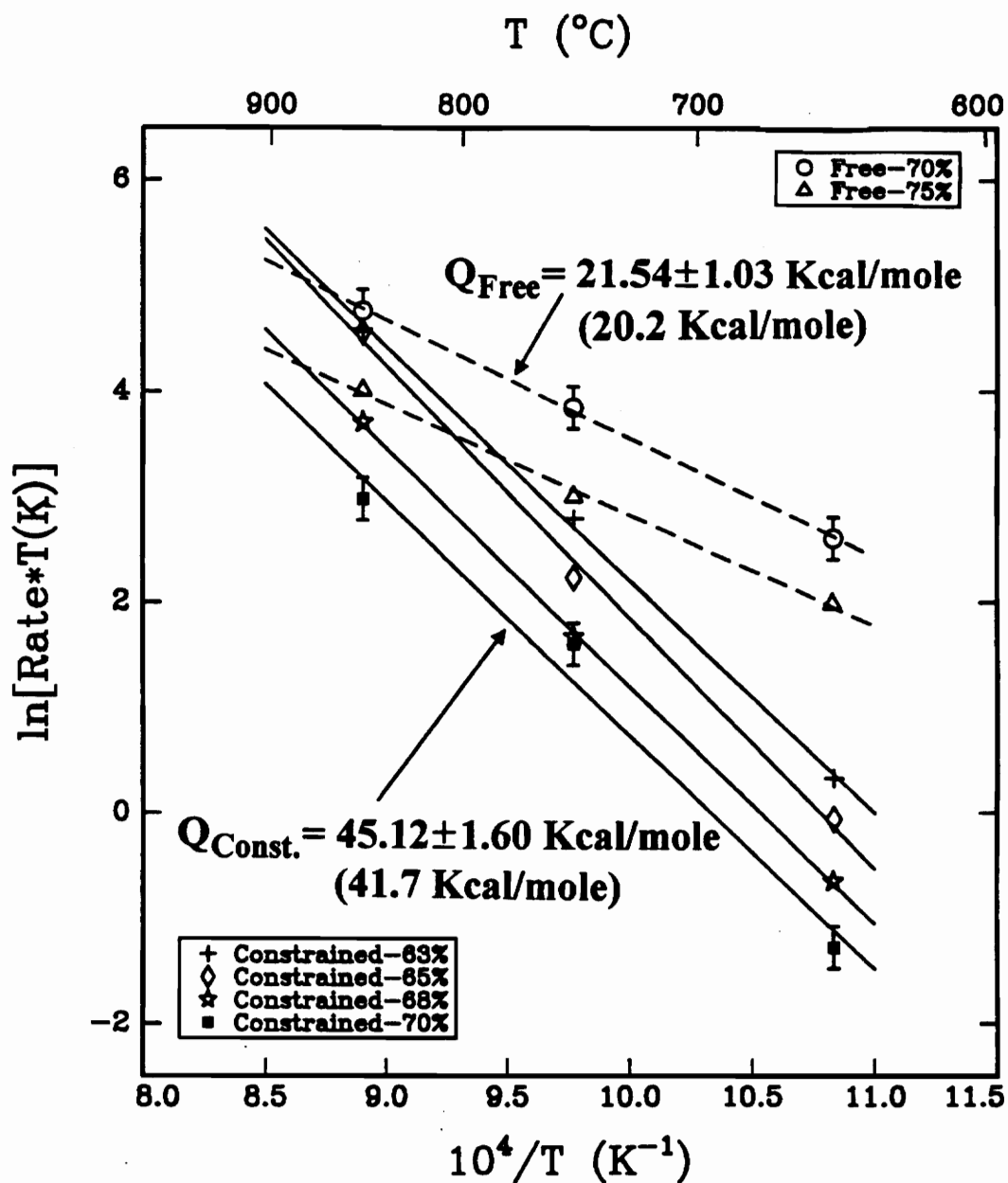
Fig.5.5   Plot of $\ln(\dot{\rho}T)$ vs. (1/T) for various relative densities of
constrained and free Au films. The slope from a linear fit to the
data at constant density, yields the activation energy for the
densification process.

that the microstructures for a particular relative density was uniform, even with different sintering times and temperatures. Figure 5.6(a) and (b) shows the SEM micrographs of constrained gold films with relative densities, $\overline{\rho}$, of 0.70. A qualitative comparison of the two micrographs revealed uniform microstructures between the two samples, although the two constrained-film samples had been subjected to different sintering times and temperatures. Figure 5.7(a) and (b) shows the SEM micrographs of freestanding gold films with relative densities, $\overline{\rho}$, of 0.80. As was the case in the constrained-films samples, the microstructures of the two freestanding film samples were very much uniform with one another, although different sintering times and temperatures had been used. Hence we can conclude from our results, that the microstructure of the samples are dependent only on the relative density and not on the sintering time and temperature. It should however be noted, that the microstructure of the constrained-film samples might be slightly different from the microstructure of the free-film samples, at the same relative density.

From the plot of Figure 5.5, we determined the activation energies to be 21.54 ± 1.03 Kcal/mole and 45.12 ± 1.6 Kcal/mole for the freestanding gold films and constrained gold films respectively. These values corresponded very well with the activation energies for grain boundary diffusion (20.2 Kcal/mole) and lattice diffusion (41.70 Kcal/mole) for gold [25]. Any factor (or a combination of factors) that caused the retardation in the densification kinetics of the constrained-films, would have produced the higher activation energy observed. However it is also highly probable that the calculated activation energy obtained for the constrained-film sintering case, is due to a change in the dominant diffusion mechanism from grain boundary diffusion (in the freestanding film sample) to lattice diffusion in the constrained-films. This change in the dominant diffusion mechanism would certainly account for the observed retardation in the densification kinetics during constrained-film sintering.
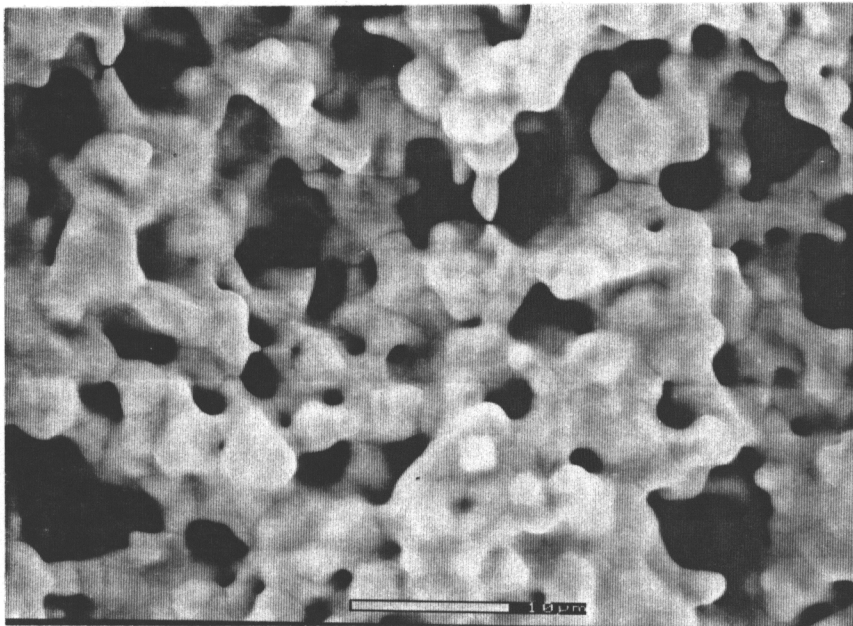
(A)
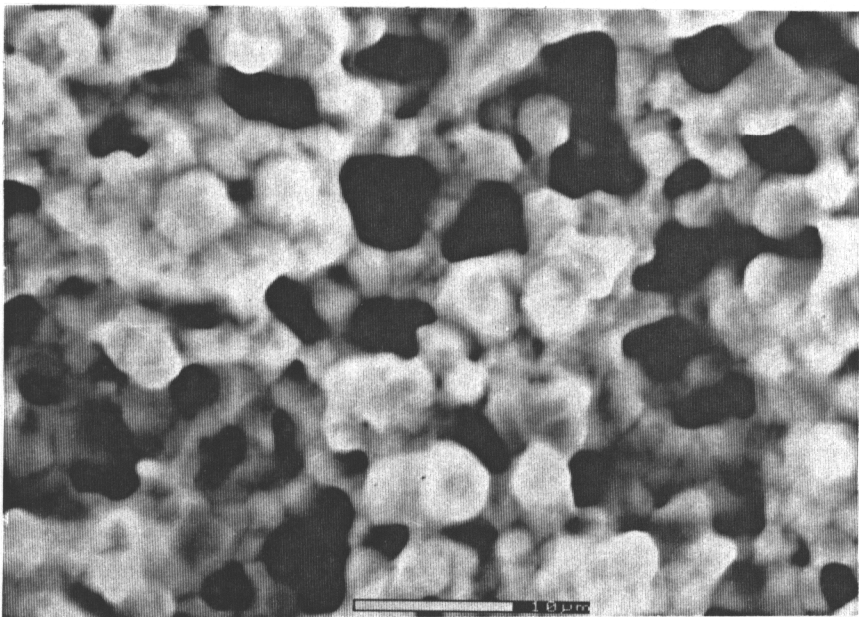
(B)

Fig.5.6   SEM micrographs of constrained gold films with $\bar{\rho} = 0.70$: (A) was

sintered at 750°C for 11 min. while (B) was sintered at 650°C for 2.5

hr. The microstructures were observed to be uniform with respect to

each other, although different sintering conditions were used
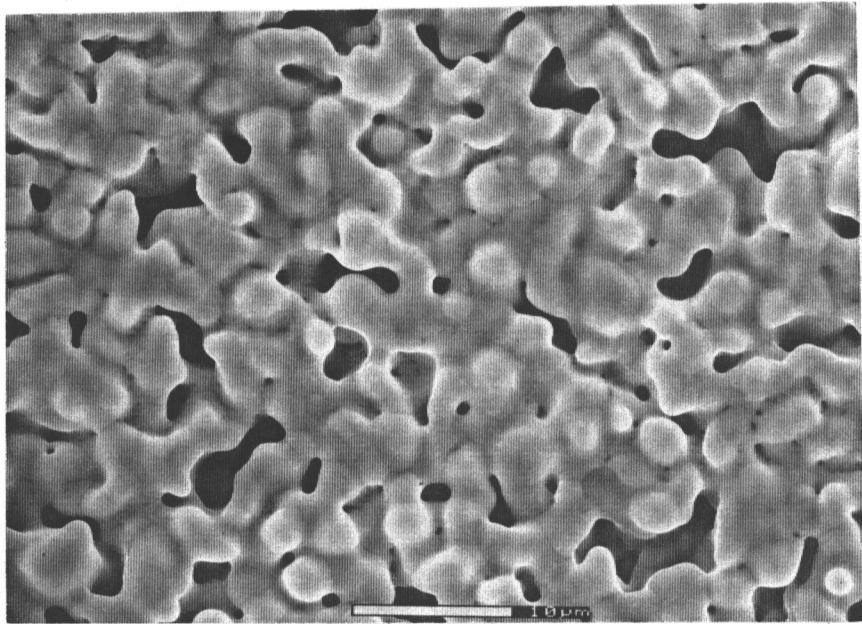
(A)
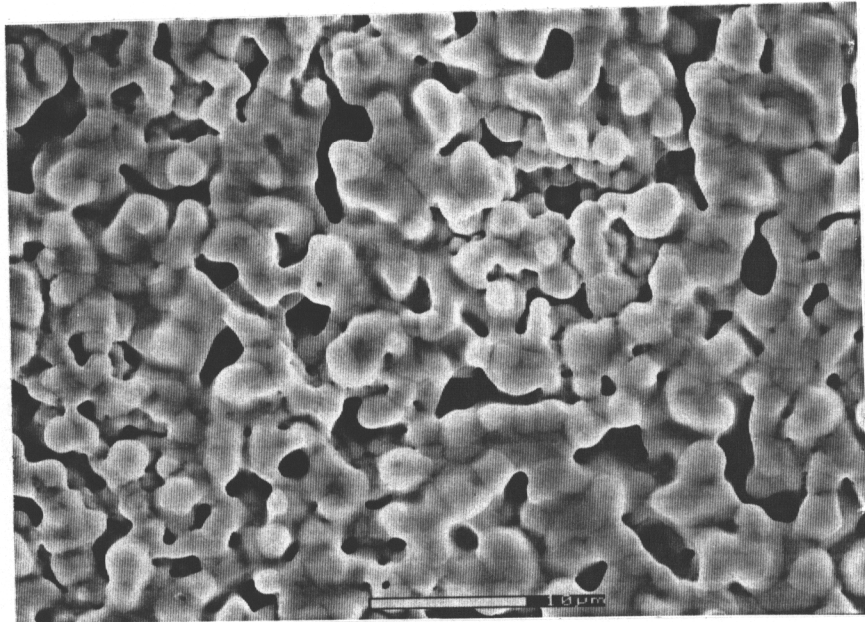
(B)

Fig.5.7   SEM micrographs of free gold films with $\overline{\rho} = 0.80$: (A) was sintered at 750°C for 8 min. while (B) was sintered at 650°C for 1/2 hr. The microstructures were observed to be uniform with respect to each other, although different sintering conditions were used

In the next section, simple schematic models of the sintering morphology are given, in order to explain the cause for the change in the dominant diffusion mechanism during constrained-film sintering.

5.4.2   A Geometrical Model Analysis

One probable reason for the retardation in the densification kinetics observed during sintering of porous gold films constrained on rigid substrates, is due to a change in the dominant diffusion mechanism from grain boundary diffusion (which is the dominant diffusion mechanism during sintering of freestanding films) to lattice diffusion. It is very possible that the physical constrain imposed on the particles by the substrate, would hinder and hence limit some of the available diffusion paths for the transport of both matter and vacancies alike. In this section, we will use schematic models of sintering morphologies in an attempt to better understand the various diffusion mechanisms at work, during the sintering of constrained and freestanding film samples.

A simple schematic diagram adapted from Bordia and Scherer [56] is given in Figure 5.8(a) and (b), to illustrate the effect of sintering porous films constrained on a rigid substrate. During the sintering of freestanding films (Figure 5.8(a)), the neck regions at A and B grows to a certain critical neck size, hence achieving mobility of the grain boundaries in those regions. The mobility of the grain boundaries contributes to the densification process, by transporting matter to the open-surface areas (mainly to the neck regions) through grain boundary diffusion. In other words, densification is achieved by transporting vacancies away from the pore regions along the grain boundaries, to the open surfaces on all sides of the freestanding film. This opposite flow of vacancies from the flow of matter in all three dimensions of the film, is the shrinkage in the x-y-z direction of the freestanding film that we observe during sintering.

However during the sintering of a porous film constrained on a rigid substrate (Figure 5.8(b)), the particles are physically constrained from coming together in the direction along the plane of the substrate. Due to this constrain, the flow of vacancies are restricted along the grain boundaries in the x-y direction along the plane of the substrate. Densification in the constrained-film is achieved only through the flow of vacancies in the direction normal to, and away from the substrate. This is deemed to be the case, since our experimental observations during sintering of constrained-films showed shrinkage only along the film thickness (in the direction normal to the substrate), while no shrinkage was observed in the x-y direction along the plane of the substrate. Since the mobility of the vacancies are restricted along the grain boundaries in the x-y direction (along neck A), its diffusion paths are limited to lattice diffusion through the bulk material as shown in Figure 5.8(b). Even if diffusion does occur through grain boundary diffusion along the neck B region, the rate limiting step of transporting matter to the neck region at B would still be through lattice diffusion.

Although the geometrical model is an oversimplification of the actual sintering process, it is still able to give an insight to the differences in the possible diffusion paths during the sintering of constrained and freestanding films. Hence it is possible to suggest based on our experimental results and the above geometrical analysis, that the retardation in the densification kinetics observed in the constrained-films is due to a change in the dominant diffusion mechanism from grain boundary diffusion to lattice diffusion.
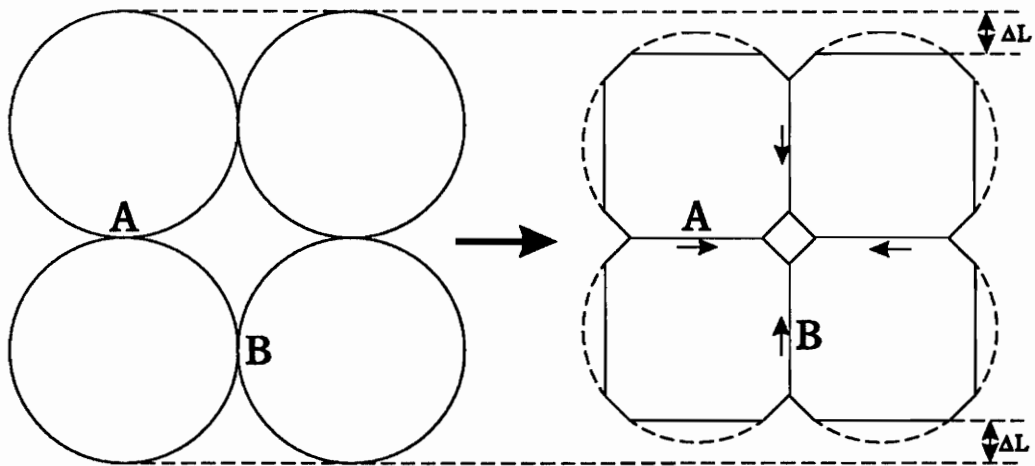
(A) Freestanding Film
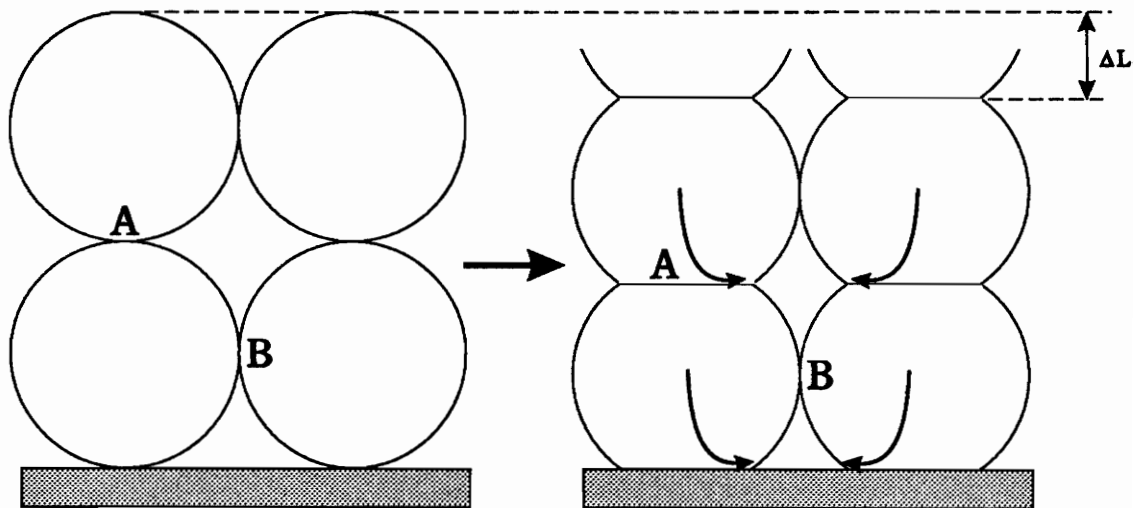
(B) Constrained Film

Fig.5.8   A schematic diagram showing the particle morphology for the

cases of free (A) and constrained (B) films during sintering. The

arrows indicates the dominating diffusion mechanism during

sintering.   (After Bordia and Scherer [56])

CHAPTER VI

SUMMARY

6.1 Conclusion

(1) We observed a significant retardation in the densification kinetics of porous gold circuit films constrained on rigid substrates, relative to the densification kinetics of freestanding porous gold circuit films, for all sintering temperatures studied.

(2) A significantly higher porosity content was found in the constrained gold circuit films due to the retarded densification kinetics. (Much higher sintering temperature are required to obtain constrained gold films as dense as the free films.)

(3) The maximum tensile stress generated within the constrained gold circuit films was determined to be about 460 KPa, during sintering at the temperature of $750^{\circ}C$.

(4) There were negligible difference in grain growth between the constrained and freestanding film samples during sintering, to account for the difference in the densification rates observed for the two samples.

(5) The activation energies calculated for the densification of freestanding gold circuit films and constrained gold circuit films, were 21.54 ± 1.03 Kcal/mole and 45.12 ± 1.60 Kcal/mole respectively. These values corresponds very well with the activation energies of grain boundary diffusion and lattice diffusion for gold respectively, as found in literature.

(6) Hence we suggest based on our experimental results, that the retardation in the densification kinetics observed during the sintering of gold circuit films constrained on rigid substrates, is due to a change in the dominant diffusion mechanism from grain boundary diffusion (freestanding films) to lattice diffusion.

6.2   Suggestions for Future Works

The present research merely represents a preliminary study in the basic understanding on the densification kinetics of films constrained on rigid substrates, that sinter by the solid state diffusion mechanism. In order to better understand the basic mechanisms that are involved during constrained-film sintering, some suggestions for the areas in which further work should focus on are given below.

(1)   The effect of coarsening of grains on the densification kinetics should be brought to a minimal, by studying the constrained sintering of ceramic films such as ZnO which has a smaller grain growth rate as compared to metals.

(2)   If the observed retardation in the densification kinetics of constrained-films are due to a change in the dominant diffusion mechanism from grain boundary diffusion to lattice diffusion, the use of plate-like particles instead of spherical particles in the constrained-films, should show an increase in the densification rates during the sintering process due to a decrease in the diffusion paths through the lattice.

(3)   The shear viscosity, G_p, and bulk viscosity, K_p, profiles should be determined using the tensile stress measurements. This profiles can then be used to develop mathematical models using viscous constitutive equations, to predict the densification profiles of constrained-film sintering from the measured densification profiles of freestanding films.

APPENDIX A

Mathematical Modeling of Constrained-Film Densification Kinetics

Using Published Results of G_p and K_p

A.1 Constitutive Relations

This section presents an earlier work done, in using published values [23,34,35,36] of the shear viscosity, G_p, and the bulk viscosity, K_p, to develop mathematical expressions that would allow the densification kinetics in a constrained material to be calculated from the experimental measurements of its free densification kinetics. The derivation of the mathematical expressions were based on the viscous analysis of an isotropic porous sintering body, where the constitutive equations relating stresses and strain rates were presented in an earlier section in equations (5.7.1), (5.7.2), & (5.7.3). For easy reference, the constitutive equations are presented again below,

$$\dot{\varepsilon}_x = \dot{\varepsilon}_f + E_p^{-1}\left[\sigma_x - v_p(\sigma_y + \sigma_z)\right] \tag{A.1.1}$$

$$\dot{\varepsilon}_y = \dot{\varepsilon}_f + E_p^{-1}\left[\sigma_y - v_p(\sigma_x + \sigma_z)\right] \tag{A.1.2}$$

$$\dot{\varepsilon}_z = \dot{\varepsilon}_f + E_p^{-1}\left[\sigma_z - v_p(\sigma_x + \sigma_y)\right] \tag{A.1.3}$$

where $\dot{\varepsilon}_x$, $\dot{\varepsilon}_y$, and $\dot{\varepsilon}_z$; and σ_x, σ_y, and σ_z are the strain rates and principle stresses respectively, while $\dot{\varepsilon}_f$ is the rate of free linear strain from unconstrained sintering. The function E_p represents uniaxial viscosity, while the Poisson's ratio is given by v_p. During constrained-film sintering, densification is allowed only in the z-direction normal to the substrate, while shrinkage along the direction of the plane is restricted (hence $\dot{\varepsilon}_x = 0$, $\dot{\varepsilon}_y = 0$). This constrain would result in a tensile stress ($\sigma = \sigma_x = \sigma_y$) being developed, while no stress is experienced in the z-direction ($\sigma_z = 0$). Using either

equations (A1.1) or (A1.2), an expression for the tensile stress in terms of the E_p, v_p; and $\dot{\varepsilon}_f$ is given by

$$\sigma = \frac{-\dot{\varepsilon}_f E_p}{(1-v_p)} \qquad (A.2)$$

Letting $\sigma_z = 0$, and $\sigma_x = \sigma_y = \sigma$, and substituting equation (A.2) into equation (A.1.3), we obtain the expression

$$[\dot{\varepsilon}_z]_c = \frac{(1+v_p)}{(1-v_p)} \dot{\varepsilon}_f \qquad (A.3)$$

which relates the strain rate in the z-direction during constrained sintering, to the rate of free linear strain during unconstrained sintering. The uniaxial viscosity and the Poisson's ratio are related to the shear and bulk viscosities, G_p and K_p, by [47]

$$E_p = \frac{9K_pG_p}{(3K_p+G_p)} \quad , \quad v_p = \frac{(3K_p-2G_p)}{[2(3K_p+G_p)]} \qquad (A.4)$$

or $\qquad K_p = \frac{E_p}{[3(1-2v_p)]} \quad , \quad G_p = \frac{E_p}{[2(1+v_p)]} \qquad (A.5)$

Defining the strains by the natural or true strain, ε, given by $\ln(w_f / w_i)$, where w_f and w_i are the respective final and initial dimensions, we establish the relation between the densification rate ($[\dot{\rho}/\rho]_c = -\dot{\varepsilon}_z$) of the constrained body and that ($[\dot{\rho}/\rho]_f = -3\dot{\varepsilon}_f$) of the free body given by

$$\left[\frac{\dot{\rho}}{\rho}\right]_c = \frac{(1+v_p)}{3(1-v_p)}\left[\frac{\dot{\rho}}{\rho}\right]_f = \frac{3K_p}{(3K_p+4G_p)}\left[\frac{\dot{\rho}}{\rho}\right]_f \qquad (A.6)$$

Hence if we are able to determine the bulk viscosity, K_p, and the shear viscosity, G_p, profiles of the material during the sintering process, then the densification kinetics in a constrained material can be calculated from the experimental measurements of its free densification kinetics by using the relation in equation (A.6).

In the next section, the densification kinetics in a constrained material will be calculated from the experimentally measured densification kinetics of its free material, using the published results of K_p and G_p profiles [23,34,35,36]. The accuracy of the mathematical models in predicting the densification kinetics of a constrained material from the densification kinetics of its free material will be determined, by comparing the calculated densification profiles with actual experimental measurements.

A.2   A Comparison of Different Mathematical Models

In the first mathematical model studied, Skorokhod's [34] model for the shear and bulk viscosities of a porous body, G_p and K_p respectively, were based experimentally on materials that sinter by solid state diffusion. The expression relating G_p and K_p to the relative density, $\overline{\rho}$, during sintering is given below as,

$$G_p = \overline{\rho}^2 \cdot \eta \quad , \quad K_p = \frac{4\eta\overline{\rho}^3}{3(1-\overline{\rho})} \tag{A.7}$$

Thus substituting the above relation of G_p and K_p with respect to the relative density, $\overline{\rho}$, into equation (A.6), we were able to calculate the densification rate of the constrained material from the measured densification kinetics of the unconstrained material.

In the second model studied, Scherer [23] used a microstructural model for modeling viscous sintering behavior of porous glasses to derive expressions for uniaxial porosity and Poisson's ratio, E_p and v_p respectively, given by:

$$E_p \approx \frac{3\eta\bar{\rho}}{(3-2\bar{\rho})} \quad , \quad v_p \approx \frac{1}{2}\left(\frac{\bar{\rho}}{3-2\bar{\rho}}\right)^{1/2} \qquad (A.8)$$

substituting the above expression into equation (A.5), we obtain expressions for G_p and K_p as follows:

$$G_p = \frac{3\eta\bar{\rho}}{6-4\bar{\rho}+(3\bar{\rho}-2\bar{\rho}^2)^{1/2}} \quad , \quad K_p = \frac{\eta\bar{\rho}}{3-2\bar{\rho}-(3\bar{\rho}-2\bar{\rho}^2)^{1/2}} \qquad (A.9)$$

The mathematical models of Venkatachari and Raj[14], and Rahaman et.al. [36], have expressions of G_p and K_p derived from sinter forging experiments of Magnesia doped Alumina powder compacts, and Cadmium Oxide (CdO) powder compacts respectively. The experimentally derived expressions for G_p and K_p, for Venkatachari and Raj's model is given as:

$$G_p = \frac{\bar{\rho}d^3}{3B_e} \quad , \quad K_p = -\frac{d^3}{B_e\bar{\rho}}\left[\ln(1-\bar{\rho})+0.5\bar{\rho}(\bar{\rho}+2)\right] \qquad (A.10)$$

where B_e is a constant which depends only on temperature, and d is the instantaneous value of the grain size.

For the model derived from Rahaman et.al. [35], the expressions for G_p and K_p are given by:

$$G_p = \frac{d^3}{A}\bar{\rho}\exp(-2a_o(1-\bar{\rho})) \quad , \quad K_p = \frac{d^3}{A}\bar{\rho}\exp(-a_o(1-\bar{\rho})) \qquad (A.11)$$

whereby d is the instantaneous grain size and A depends on the transport properties of the material; the constant a_0 was evaluated experimentally, depending on the slope of the densification rate.

A.3   Mathematical Models vs. Experimental Results : A Comparison

Densification profiles of constrained-film calculated from different mathematical models [23,34,35,36], are compared with the densification profiles of the constrained gold thick film determined experimentally in Figure (A.1). In the figure shown, all of the models seemed to overestimate the densification kinetics of the constrained-film. The models derived from Scherer [23] (curve 2) and Skorokhod [34] (curve 3), showed very close matching with each other. This was expected since the close resemblance was also observed in the shear viscosity, G_p, dependence on relative density. Although both models by Rahaman et.al. [35] (curves 1a and 1b), and Venkatachari and Raj [36] (curve 4) were derived experimentally from sinter forging experiments, the calculated densification kinetics of the constrained-film were very different from each other. This difference in the densification profiles predicted, could have been due to the different conditions at which the two sinter forging experiments were conducted in the derivation of the shear and bulk viscosities, G_p and K_p respectively. Venkatachari and Raj [36] used axial loads that were greater than the intrinsic sintering pressure, while Rahaman et.al. [35] used axial loads that were smaller than the intrinsic sintering pressure.

From the comparison of the mathematical models with the experimentally measured densification profiles, we can clearly see that the models are not able to accurately calculate the densification kinetics of constrained material from the densification kinetics of its free material. Hence a better modal with more accurate profiles of G_p and K_p are required to give more accurate predictions.
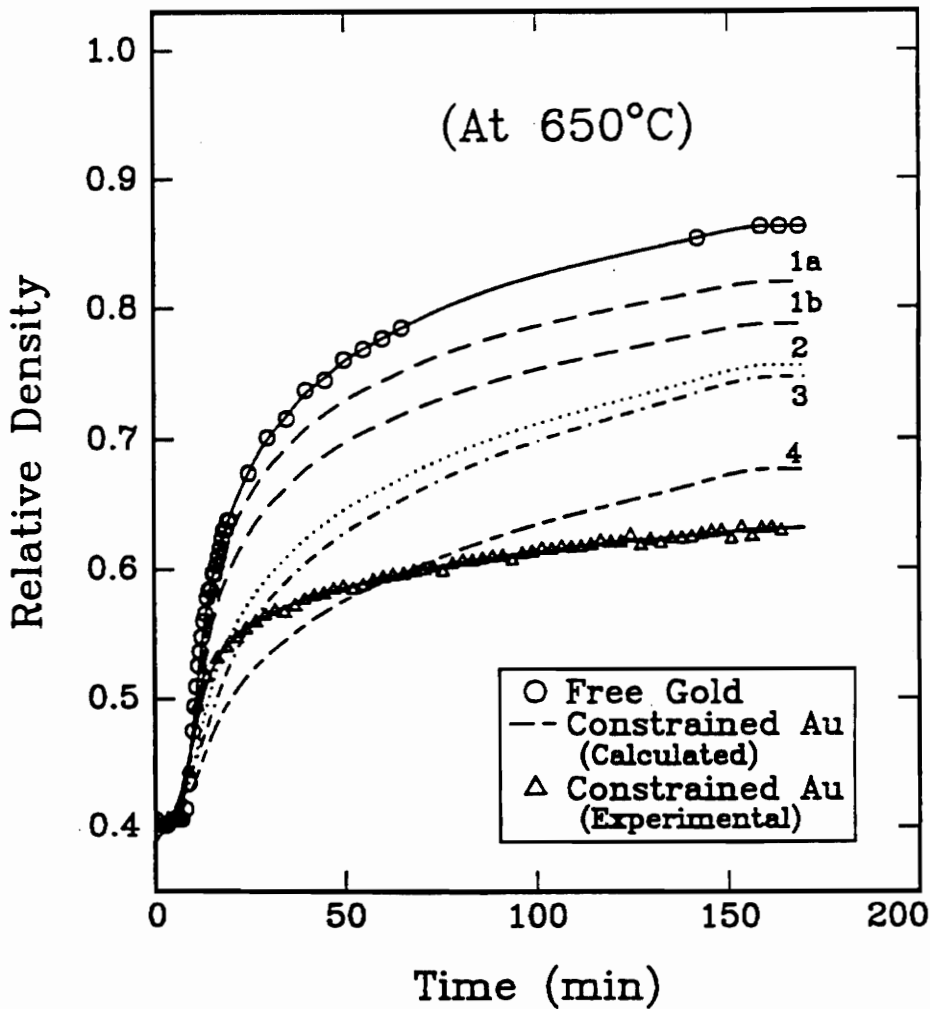
Fig.A.1   Plot of Relative Density vs. Sintering Time of DuPont Au films

sintered at 650 °C. Curve labels: 1a = Rahaman et.al's model [35] (densification kinetics is not compensated for grain growth); 1b = Rahaman et.al's. model [35] (densification kinetics is compensated for grain growth); 2 = Scherer's model [23]; 3 = Skorokhod's model [34]; 4 = Venkatachari and Raj's model [36]. Otherwise stated, the models are not compensated for grain growth.

REFERENCES

[1]   R.R. Tummala, Microelectronics Packaging Handboo, edited by R.R.
        Tummala and E.J. Rymaszewaki (Van Nostrand Reinhold, New York, 1989),
        Chapter 7.

[2]   G-Q. Lu, R.C. Sutterlin, T.K. Gupta, "Effects of Mismatched Sintering
        Kinetics on Camber in a Low Temperature Cofired Ceramic Package,"
        J. Am. Ceram Soc, **76**, [8] 1907-1914   (1993).

[3]   P.J. Holmes and R.G. Loasby, Handbook of Thick Film Technology,
        Electrochemical Publications Limited, Scotland, (1976).

[4]   R.C. Sutterlin, G-Q Lu, and T.K. Gupta, "Cosintering of Gold/LTCC substrates:
        Development of camber and via defects.", *Ceramic Trans.*, **33**,   (1993)

[5]   B. Schwartz and D.L. Wilcox, *Proceedings of the Electronic Components
        Conference, IEEE*, New York, **17**,   (1967).

[6]   R.E. Mistler, D.J. Shanefield and R.B. Runk, Ceramic Processing Before Firing,
        edited by G.Y. Onoda Jr. and L.L. Hench, John Wiley & Sons, New York, N.Y.
        411,   (1978).

[7]   J.Pepin, W.Borland, P.O'Callaghan and R. Young, *1988 Capacitor and Resistor
        Technology Symposium Proceedings*, **54**,   (1988).

[8]   G.C. Kuczynski, "Self - Diffusion in Sintering of Metallic Particles", *Metals
        Trans.*, 169   (1949).

[9]   F. Thummler and W. Thomma, "The Sintering Process", *Met. Reviews*, **12**:69
        (1967).

[10]   R.L. Coble and R.M. Canon, "Current Paradigms in Powder Processing in :
        Processing of Crystalline Ceramics", *Mat. Science Research*, **11**,   Palmour,
        Davis and Hare, eds., Plenum Press, New York (1978).

[11]   G. Gessinger, "Some Aspects on Progress and Future Trends in Sintering
        Theory", *Powder Met. Int.*, **1**:15   (1969).

[12]   W.D. Kingery, Kinetics of High Temperature Process, The Technology Press
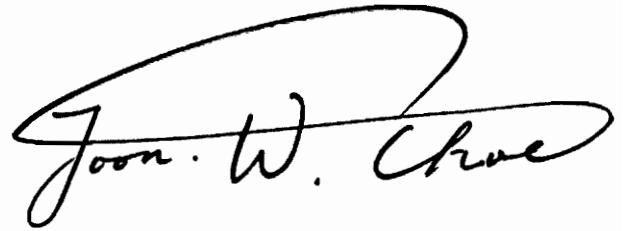   of Mass. Inst. of Tech. and J. Wiley & Sons, New York, (1958).

[13]   M.F. Ashby, "A First Report On Sintering Diagrams", *Acta. Metall.*, **22**, 275 (1974)

[14]   R.L. Coble, "Sintering Crystalline Solids II.: Experimental Test of Diffusion Models in Powder Compacts", *J. Appl. Phys.*, **32**, 787 (1961).

[15]   D.L. Johnson,"A General Model for the Intermediate Stage of Sintering.", *J. Am. Ceram. Soc.*, **53**, 574 (1970).

[16]   W. Beere,"The Second Stage Sintering Kinetics of Powder Compacts", *Acta Metall.*, **23**, 139 (1975).

[17]   E.g. the dilatometer made by Netzsch, Exton, P.A.;

[18]   E.g. the TMA made by Du Pont Instruments, Wilmington, DE.;

[19]   Milton Ohring, The Material Science of Thin Films, Academic Press, Inc. (1992).

[20]   R.M. Christensen, Theory of Viscoelasticity, An Introduction, 2nd Edn.; Academic Press, New York, (1982).

[21]   G.W. Scherer, Relaxation in glass and Composites, Wiley-Interscience, New York, (1986).

[22]   S.P. Timoshenko and J.N. Goodier, Theory of Elasticity, 3rd edition, McGraw-Hill, New York, (1970).

[23]   G.W. Scherer, "Sintering Inhomogeneous Glasses: Application to Optical Waveguides", *J. Non-Crys. Solids*, **34**, 239-56 (1979).

[24]   T.Cheng, "Co-sintering Behavior of Ceramic-Metal and Glass-Metal Multilayer Films : Modelling and Experiments", Ph.D Thesis. Cornell University, Ithaca, NY, (1989).

[25]   E.A. Brandes, Smithells Metals Reference Book, Sixth Edition, Butterworth & Co (Publishers) Ltd (1983).

[26]   R.A. Gardner and R.W. Nufer, *Solid State Technology*, **38**, [5] (1974).

[27]   A.H. Kumar and R.R Tummala, "State-Of-The-Art, Glass-Ceramic/Copper, Multilayer Substrate For High performance Computers.", *Int. J. for Hybrid Microelectronics*, **14**, 137 (1991).

[28]   W.D. Kingery, H.K. Bowen, and D.R. Uhlmann, Introduction to Ceramics, 2nd Edition, John Wiley & Sons, New York, (1976).

[29]   R.B. Hammer, D.O. Powell, S. Mukherjee, R. Tummala, and R. Raj.,
"Ceramics in Electronic Packaging", p 323 in Principles of Electronic Packaging,
edited by D.P. Seraphim, R.C. Lasky, and C-Y. Li, McGraw-Hill Book Co.,
New York, (1989).

[30]   C.P. Ostertag, "Technique for Measuring Stresses which occur during Sintering
of a Fiber-Reinforced Ceramic Composite.", *J. Am. Ceram. Soc.*,
70, [12] C355-C357 (1987).

[31]   K.R. Mikeska, G.W. Scherer, and R.K. Bordia, "Constitutive Behavior of Sintering
Materials", *Ceramic Transactions*, **7**, 200-214 (1990).

[32]   G.W. Scherer, "Viscous Sintering Under Uniaxial Load", *J. Am. Ceram. Soc.*, **69**,
[9] C-206-C-207 (1986).

[33]   G.W. Scherer, "Viscous Sintering of Particle-Filled Composites", *Ceramic Bulletin*,
70, [6] 1059-63 (1991).

[34]   V.V. Skorokhod, *Poroshk. Metall.*, **2**, 14 (1961).

[35]   M.N. Rahaman, L.C. De Jonghe, and R.J. Brook, "Effect of Shear Stress on
Sintering", *J. Am. Ceram. Soc.*, **69**, [1] 53-58 (1986).

[36]   K.R. Venkatachari and R. Raj., "Shear Deformation and Densification of Ceramic
Compacts", *J. Am. Ceram. Soc.*, **69**, [6] 499-506 (1986).

[37]   R. Raj, "Analysis of the Sintering Pressure", *J. Am. Ceram. Soc.*, **70**, [9] C210
(1987).

[38]   M.N. Rahaman and L.C. DeJonghe, "Effect of Rigid Inclusions on the Sintering of
Glass Powder Compacts", *J. Am. Ceram. Soc.*, **70**, [12] C348   (1987).

[39]   G.W. Scherer, "Sintering with Rigid Inclusions", *J. Am. Ceram. Soc.*, **70**, [10]
719-25 (1987).

[40]   A.G. Evans, "Considerations of Inhomogeneity Effects in Sintering", *J. Am.
Ceram. Soc.*, **65**, [10] 497 (1982).

[41]   C.H. Hsueh, A.G. Evans, R.M. Cannon, and R.J. Brook, "Viscoelastic Stresses
and Sintering Damage In Heterogeneous Powder Compacts", *Acta. Metall.*, **34**,
[5] 927 (1986).

[42]   L.C. DeJonghe, M.N. Rahaman and C.H. Hsueh, "Transient Stresses In Bimodal
Compacts During Sintering", *Acta. Metall.*, **34**, [7] 1467 (1986).

[43]   R. Raj and R.K. Bordia, "Sintering Behavior of Bi-modal Powder Compacts,"
       Acta Metall., **32**, [7] 1003-19 (1984).

[44]   L.C. DeJonghe and M.N. Rahaman, "Sintering Stress Of Homogeneous And
       Heterogeneous Powder Compacts", *Acta Metall.*, **36**, [1] 223 (1988).

[45]   G.W. Scherer, "Viscous Sintering of a Bimodal Pore-Size Distribution", *J. Am.
       Ceram. Soc.*, **67**, [11] 709 (1984).

[46]   R.K. Bordia and R.Raj, "Sintering of $TiO_2 - Al_2O_3$ Composites : A Model
       Experimental Investigation", *J. Am. Ceram. Soc.*, **71**, [4] 302 (1988).

[47]   R.K. Bordia and G.W. Scherer, "On Constrained Sintering - I. Constitutive
       Model for a Sintering Body", *Acta Metall.*, **36**, [9] 2393-97 (1988).

[48]   R.K. Bordia and G.W. Scherer, "On Constrained Sintering - II. Comparison of
       Constitutive Models", *Acta Metall.*, **36**, [9] 2399-2409 (1988).

[49]   R.K. Bordia and G.W. Scherer, "On Constrained Sintering - III. Rigid Inclusions",
       Acta Metall., **36**, [9] 2411-2416 (1988).

[50]   G.W. Scherer and T.J. Garino, "Viscous Sintering on a Rigid Substrate", *J. Am.
       Ceram. Soc.*, **68**, [4] 216-20 (1985).

[51]   T.J. Garino and H.K. Bowen, "Kinetics of Constrained-film Sintering", *J. Am
       Ceram.Soc.*, **73**, [2] 251-257 (1990).

[52]   R.K. Bordia and R. Raj, "Sintering Behavior of Ceramic Films Constrained by a
       Rigid Substrate", *J. Am. Ceram Soc.*, **68**, [6] 287-92 (1985).

[53]   C.H. Hsueh, "Sintering Of A Ceramic Film On A Rigid Substrate", *Scripta Metall.*,
       19, 1213-1217 (1985).

[54]   A.G. Evans and C.H. Hsueh, "Behavior of Large Pores During Sintering and Hot
       Isostatic Pressing", *J. Am. Ceram. Soc.*, **69**, [6] 444-448 (1986).

[55]   R.K. Bordia and G.W. Scherer, "Sintering Composites : A Critique Of The
       Available Analyses", *Ceram. Trans.*, **1**, 872-886 (1988).

[56]   R.K. Bordia and R. Raj, "Hot Isostatic Pressing of Ceramic/Ceramic Composites
       at Pressures < 10 MPa", *Adv. Ceram. Mater.*, **3**, 122 (1988).

VITA

The author is a native of the Republic of Korea, born on August 18th, 1969. He lived in Singapore since the age of 5, where he attended the National Junior College in Singapore from 1985-1987. He attended Carnegie Mellon University where he received a Bachelor of Science Degree in Metallurgical Engineering and Materials Science in December of 1991. In the fall of 1992, he came to Virginia Polytechnic Institute and State University to pursue graduate studies in the field of Materials Science and Engineering. He received a Master of Science Degree from Virginia Polytechnic Institute and State University in July, 1994.